Article

Quantum phases of matter on a 256-atom programmable quantum simulator

https://doi.org/10.1038/s41586-021-03582-4

Received: 21 December 2020

Accepted: 26 April 2021

Published online: 7 July 2021

Check for updates

Sepehr Ebadi[1], Tout T. Wang[1], Harry Levine[1], Alexander Keesling[1,2], Giulia Semeghini[1], Ahmed Omran[1,2], Dolev Bluvstein[1], Rhine Samajdar[1], Hannes Pichler[3,4], Wen Wei Ho[1,5], Soonwon Choi[6], Subir Sachdev[1], Markus Greiner[1], Vladan Vuletić[7] & Mikhail D. Lukin[1]✉

Motivated by far-reaching applications ranging from quantum simulations of complex processes in physics and chemistry to quantum information processing[1], a broad effort is currently underway to build large-scale programmable quantum systems. Such systems provide insights into strongly correlated quantum matter[2–6], while at the same time enabling new methods for computation[7–10] and metrology[11]. Here we demonstrate a programmable quantum simulator based on deterministically prepared two-dimensional arrays of neutral atoms, featuring strong interactions controlled by coherent atomic excitation into Rydberg states[12]. Using this approach, we realize a quantum spin model with tunable interactions for system sizes ranging from 64 to 256 qubits. We benchmark the system by characterizing high-fidelity antiferromagnetically ordered states and demonstrating quantum critical dynamics consistent with an Ising quantum phase transition in (2 + 1) dimensions[13]. We then create and study several new quantum phases that arise from the interplay between interactions and coherent laser excitation[14], experimentally map the phase diagram and investigate the role of quantum fluctuations. Offering a new lens into the study of complex quantum matter, these observations pave the way for investigations of exotic quantum phases, non-equilibrium entanglement dynamics and hardware-efficient realization of quantum algorithms.

Recent breakthroughs have demonstrated the potential of programmable quantum systems, with system sizes reaching around 50 trapped ions[2,15,16] or superconducting qubits[7–9], for simulations and computation. Correlation measurements with over 70 photons have been used to perform boson sampling[10], while optical lattices with hundreds of atoms are being used to explore Hubbard models[3–5]. Larger-scale Ising spin systems have been realized using superconducting elements[17], but they lack the coherence essential for probing quantum matter.

Neutral atom arrays have recently emerged as a promising platform for realizing programmable quantum systems[6,12,18]. Based on individually trapped and detected cold atoms in optical tweezers with strong interactions between Rydberg states[19], atom arrays have been used to explore quantum dynamics in one- and two-dimensional (1D and 2D) systems[6,20–24], to create high-fidelity[25] and large-scale[26] entanglement, to perform parallel quantum logic operations[27,28], and to realize optical atomic clocks[29,30]. Although large numbers of atoms have been trapped[30] and rearranged in two and three dimensions[31–34], coherent manipulation of programmable, strongly interacting systems with more than 100 individual particles remains a challenge. Here, we realize a programmable quantum simulator using arrays of up to 256 neutral atoms with tunable interactions, demonstrating several new quantum phases and quantitatively probing the associated phase transitions.

Programmable Rydberg arrays in 2D

Our experiments are carried out on the second generation of an experimental platform described previously[6]. The new apparatus uses a spatial light modulator (SLM) to form a large 2D array of optical tweezers in a vacuum cell (Fig. 1a, Methods). This static tweezer array is loaded with individual ^{87}Rb atoms from a magneto-optical trap, with a uniform loading probability of 50–60% across up to 1,000 tweezers. We rearrange the initially loaded atoms into programmable, defect-free patterns using a second set of moving optical tweezers that are steered by a pair of crossed acousto-optical deflectors (AODs) to arbitrary positions in two dimensions (Fig. 1a)[35]. Our parallel rearrangement protocol (see Methods) enables rearrangement into a wide variety of geometries including square, honeycomb and triangular lattices (left panels in Fig. 1b–d). The procedure takes a total time of 50–100 ms for arrays of up to a few hundred atoms and results in filling fractions exceeding 99%.

Qubits are encoded in the electronic ground state $|g\rangle$ and the highly excited $n = 70$ Rydberg state $|r\rangle$ of each atom. We illuminate the entire array from opposite sides with two counter-propagating laser beams at 420 nm and 1,013 nm, shaped into light sheets (see Methods), to coherently couple $|g\rangle$ to $|r\rangle$ via a two-photon transition (Fig. 1a).

[1]Department of Physics, Harvard University, Cambridge, MA, USA. [2]QuEra Computing Inc., Boston, MA, USA. [3]Institute for Theoretical Physics, University of Innsbruck, Innsbruck, Austria. [4]Institute for Quantum Optics and Quantum Information, Austrian Academy of Sciences, Innsbruck, Austria. [5]Department of Physics, Stanford University, Stanford, CA, USA. [6]Department of Physics, University of California Berkeley, Berkeley, CA, USA. [7]Department of Physics and Research Laboratory of Electronics, Massachusetts Institute of Technology, Cambridge, MA, USA. ✉e-mail: lukin@physics.harvard.edu

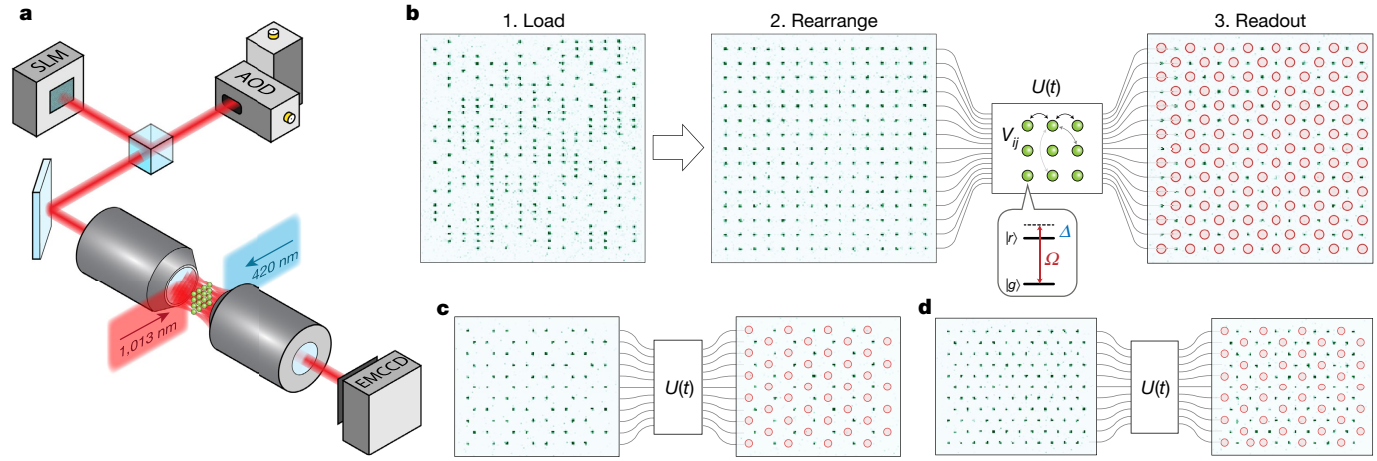

Fig. 1 | Programmable two-dimensional arrays of strongly interacting Rydberg atoms. a, Atoms are loaded into a 2D array of optical tweezer traps and rearranged into defect-free patterns by a second set of moving tweezers. Lasers at 420 nm and 1,013 nm drive a coherent two-photon transition in each atom between ground state $|g\rangle = |5S_{1/2}, F = 2, m_F = -2\rangle$ and Rydberg state $|r\rangle = |70S_{1/2}, m_j = -1/2, m_I = -3/2\rangle$. EMCCD, electron-multiplying charge-coupled device. **b**, Fluorescence image of initial random loading of atoms, followed by rearrangement to a defect-free 15 × 15 (225 atoms) square array. After this initialization, the atoms evolve coherently under laser excitation according to the Hamiltonian (equation (1)) with Rabi frequency $\Omega(t)$, detuning $\Delta(t)$ and long-range interactions V_{ij}, realizing a many-body unitary $U(t)$. Finally, the state of each atom is read out, with atoms excited to $|r\rangle$ detected as loss and marked with red circles. Shown on the far right is an example measurement following quasi-adiabatic evolution into the chequerboard phase. **c**,**d**, Similar evolution on honeycomb and triangular lattices result in analogous ordered phases of Rydberg excitations with filling 1/2 and 1/3, respectively.

The resulting many-body dynamics $U(t)$ are governed by a combination of the laser excitation and long-range van der Waals interactions between Rydberg states ($V_{ij} = V_0/|\mathbf{x}_i - \mathbf{x}_j|^6$), described by the Hamiltonian

$$\frac{H}{\hbar} = \frac{1}{2}\sum_i (\Omega|r_i\rangle\langle g_i| + \text{h.c.}) - \Delta\sum_i n_i + \sum_{i<j} V_{ij} n_i n_j \qquad (1)$$

where $\hbar$ is the reduced Planck's constant, h.c. denotes the Hermitian conjugate, $n_i = |r_i\rangle\langle r_i|$, and Ω and Δ are the two-photon Rabi frequency and detuning, respectively. After evolution under the Hamiltonian (1), the state of each atomic qubit is read out by fluorescence imaging that detects only atoms in $|g\rangle$, while atoms in $|r\rangle$ are detected as loss. Detection fidelities exceed 99% for both states (see Methods).

The Rydberg blockade mechanism[36,37] is central to understanding the programmable dynamics driven by the Hamiltonian (1). It originates from the long-range interactions between Rydberg states, providing an effective constraint that prevents simultaneous excitation of atoms within a blockade radius $R_b \equiv (V_0/\Omega)^{1/6}$. We control the effective blockade range R_b/a by programming the lattice spacing a for the atom array. Using these control tools, we explore quantum evolution resulting in a wide variety of quantum phases.

Chequerboard phase

The smallest value of R_b/a that results in an ordered phase for the quantum many-body ground state of the system corresponds to $R_b/a \approx 1$, where only one out of every pair of nearest-neighbour atoms can be excited to $|r\rangle$. On a square array, this constraint leads to a $\mathbb{Z}_2$-symmetry-broken chequerboard phase with an antiferromagnetic (AF) ground state. To realize such a state, we initialize the array at $R_b/a = 1.15$ ($a = 6.7$ μm, $\Omega = 2\pi \times 4.3$ MHz) with all atoms in $|g\rangle$. We then dynamically sweep the detuning Δ from negative to positive values while keeping the Rabi frequency Ω fixed to bring the system quasi-adiabatically into the chequerboard phase (Fig. 1b and Fig. 2a). A similar approach can be used to create analogous ordered phases on other lattice geometries (Fig. 1c, d).

We quantify the strength of antiferromagnetic correlations in the chequerboard phase over many experimental repetitions using the connected density–density correlator $G^{(2)}(k,l) = \frac{1}{N_{(k,l)}}\sum_{i,j}(\langle n_i n_j\rangle - \langle n_i\rangle\langle n_j\rangle)$, where the sum is over all pairs of atoms (i,j) separated by the same relative lattice displacement $\mathbf{x} = (k,l)$ sites, normalized by the number of such pairs $N_{(k,l)}$. Our measurement of $G^{(2)}(k,l)$ on a 12 × 12 system (Fig. 2b) yields horizontal, vertical and radially averaged correlation lengths of $\xi_H = 11.1(1)$, $\xi_V = 11.3(1)$ and $\xi_R = 12.0(1)$, respectively (see Fig. 2c and Methods), showing long-range correlations across the entire 144-atom array. These exceed the values reported previously for 2D systems[20,21] by nearly an order of magnitude.

Single-site readout also allows us to study individual many-body states of our system (Fig. 2d). Out of 6,767 repetitions on a 12 × 12 array, the two perfectly ordered states $|\text{AF}_1\rangle$ and $|\text{AF}_2\rangle$ are by far the most frequently observed microstates, with near-equal probabilities between the two. We benchmark our state preparation by measuring the probability of observing perfect chequerboard ordering as a function of system size (Fig. 2e). We find empirically that the probability scales with the number of atoms according to an exponential 0.97^N, offering a benchmark that includes all experimental imperfections such as finite detection fidelity, non-adiabatic state preparation, spontaneous emission, finite Rydberg-state lifetime and residual quantum fluctuations in the ordered state (see Methods). Remarkably, even for a system size as large as 15 × 15 (225 atoms), we still observe the perfect antiferromagnetic ground state with probability $0.10^{+5}_{-4}\%$ within the exponentially large Hilbert space of dimension $2^{225} \approx 10^{68}$.

(2 + 1)D Ising quantum phase transition

We now study the quantum phase transition into the chequerboard phase. Quantum phase transitions fall into universality classes characterized by critical exponents that determine universal behaviour near the quantum critical point, independent of the microscopic details of the Hamiltonian[13]. The transition into the chequerboard phase is expected to be in the paradigmatic—but never previously observed—quantum Ising universality class in (2 + 1) dimensions[14]. Quantitative probing of such transitions can be used to benchmark quantum many-body evolution[38].

To explore universal scaling across this phase transition for a large system, we study the dynamical build-up of correlations associated with the quantum Kibble–Zurek mechanism[24,39] on a 16 × 16 (256 atoms) array, at fixed $R_b/a = 1.15$. We start at a large negative detuning with all atoms in $|g\rangle$ and linearly increase Δ/Ω, stopping at various points to

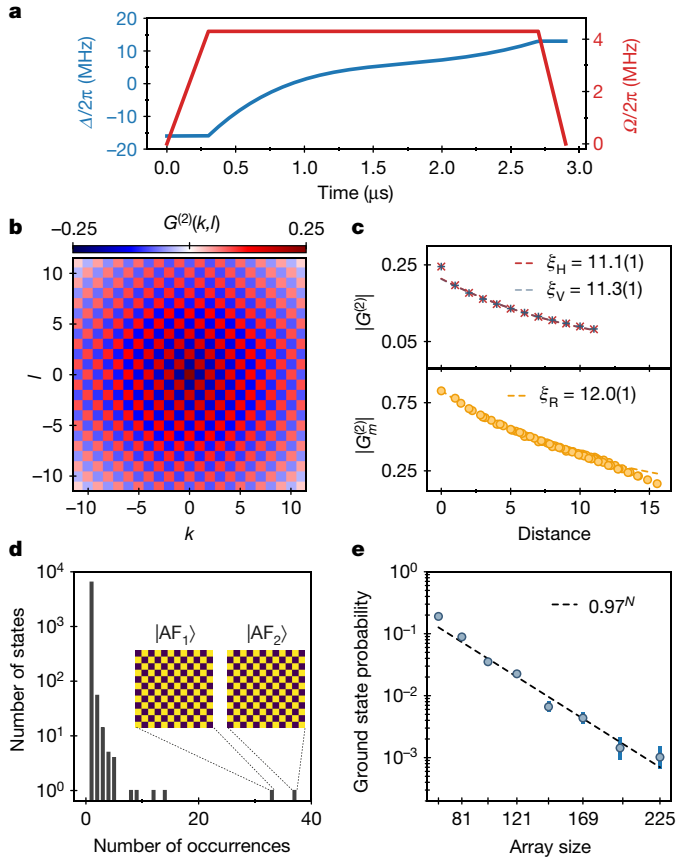

Fig. 2 | Benchmarking of quantum simulator using chequerboard ordering. **a**, A quasi-adiabatic detuning sweep $\Delta(t)$ at constant Rabi frequency Ω is used to prepare the chequerboard ground state with high fidelity. **b**, Two-site correlation function $G^{(2)}(k,l)$, averaged over all pairs of atoms on a 12 × 12 array, showing near-perfect alternating correlations throughout the entire system. **c**, Top panel: exponential fits of rectified horizontal and vertical correlations are used to extract correlation lengths in the corresponding directions, ξ_H and ξ_V. Bottom panel: radially averaged coarse-grained correlations $G^{(2)}{}_m$ as a function of radial distance used to calculate ξ_R (see Methods). Error (in brackets) denotes the uncertainty in the fit. **d**, Histogram of many-body state occurrence frequency after 6,767 repetitions of the experiment on a 12 × 12 array. The two most frequently occurring microstates correspond to the two perfect chequerboard orderings AF1 and AF2, and the next four most common ones are those with a single defect in one of the corners of the array. **e**, Probability of finding a perfect chequerboard ground state as a function of array size (error bars represent the 68% confidence interval). The slightly higher probabilities in odd × odd systems is due to commensurate edges on opposing sides of the array. All data in this figure are conditioned on defect-free rearrangement of the array.

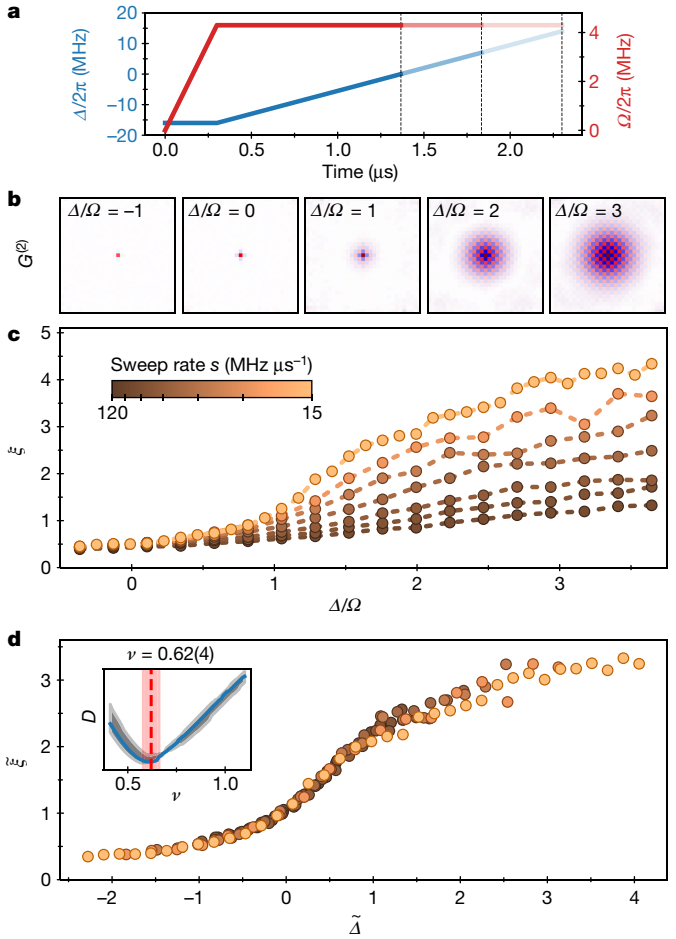

Fig. 3 | Observation of the (2 + 1)D Ising quantum phase transition on a 16 × 16 array. **a**, The transition into the chequerboard phase is explored using a linear detuning sweep $\Delta(t)$ at constant Ω. The resulting chequerboard ordering is measured at various endpoints. **b**, Example of growing correlations $G^{(2)}$ with increasing Δ/Ω along a linear sweep with sweep rate $s = 15$ MHz μs^{-1}. **c**, Growth of correlation length ξ for s spanning about an order of magnitude (15, 21, 30, 42, 60, 85 and 120 MHz μs^{-1}). ξ used here measures correlations between the coarse-grained local staggered magnetization (see Methods). **d**, For an optimized value of the critical exponent ν, all curves collapse onto a single universal curve when rescaled relative to the quantum critical point Δ_c. Inset: distance D between all pairs of rescaled curves as a function of ν (see Methods). The minimum at $\nu = 0.62(4)$ (red dashed line) yields the experimental value for the critical exponent (red and grey shaded regions indicate uncertainties) and is consistent with the theoretical prediction[14] $\nu = 0.629$.

measure the growth of correlations across the phase transition (Fig. 3a,b). Slower sweep rates $s = \mathrm{d}\Delta/\mathrm{d}t$ result in longer correlation lengths ξ, as expected (Fig. 3c).

The quantum Kibble–Zurek mechanism predicts a universal scaling relationship between the control parameter Δ and the correlation length ξ. Specifically, when both Δ and ξ are rescaled with the sweep rate s (relative to a reference rate s_0)

$$\tilde{\xi} = \xi(s/s_0)^{\mu} \tag{2}$$

$$\tilde{\Delta} = (\Delta - \Delta_c)(s/s_0)^{\kappa} \tag{3}$$

with critical point Δ_c and critical exponents $\mu \equiv \nu/(1+z\nu)$ and $\kappa \equiv -1/(1+z\nu)$, then universality implies that the rescaled $\tilde{\xi}$ versus $\tilde{\Delta}$ collapses onto a single curve[24] for any sweep rate s. Figure 3d shows a striking collapse of experimental data, demonstrating such a universal scaling.

The underlying class of phase transitions (quantum or classical) is described by Lorentz-invariant field theories[13], resulting in dynamical critical exponent $z = 1$. We experimentally extract the correlation length critical exponent ν for our system by finding the value that optimizes universal collapse. To do so, we first independently determine the position of the critical point Δ_c, which corresponds to the peak of the susceptibility $\chi = -\partial^2\langle H\rangle/\partial\Delta^2$ and is associated with a vanishing gap[13]. For adiabatic evolution under the Hamiltonian (1), the susceptibility χ is related to the mean Rydberg excitation density $\langle n\rangle$ by $\chi = \partial\langle n\rangle/\partial\Delta$ according to the Hellman-Feynman theorem. We measure $\langle n\rangle$ versus Δ along a slow linear sweep to remain as adiabatic as possible. We take the numerical derivative of the fitted data to obtain χ, finding its peak to be at $\Delta_c/\Omega = 1.12(4)$ (see Methods).

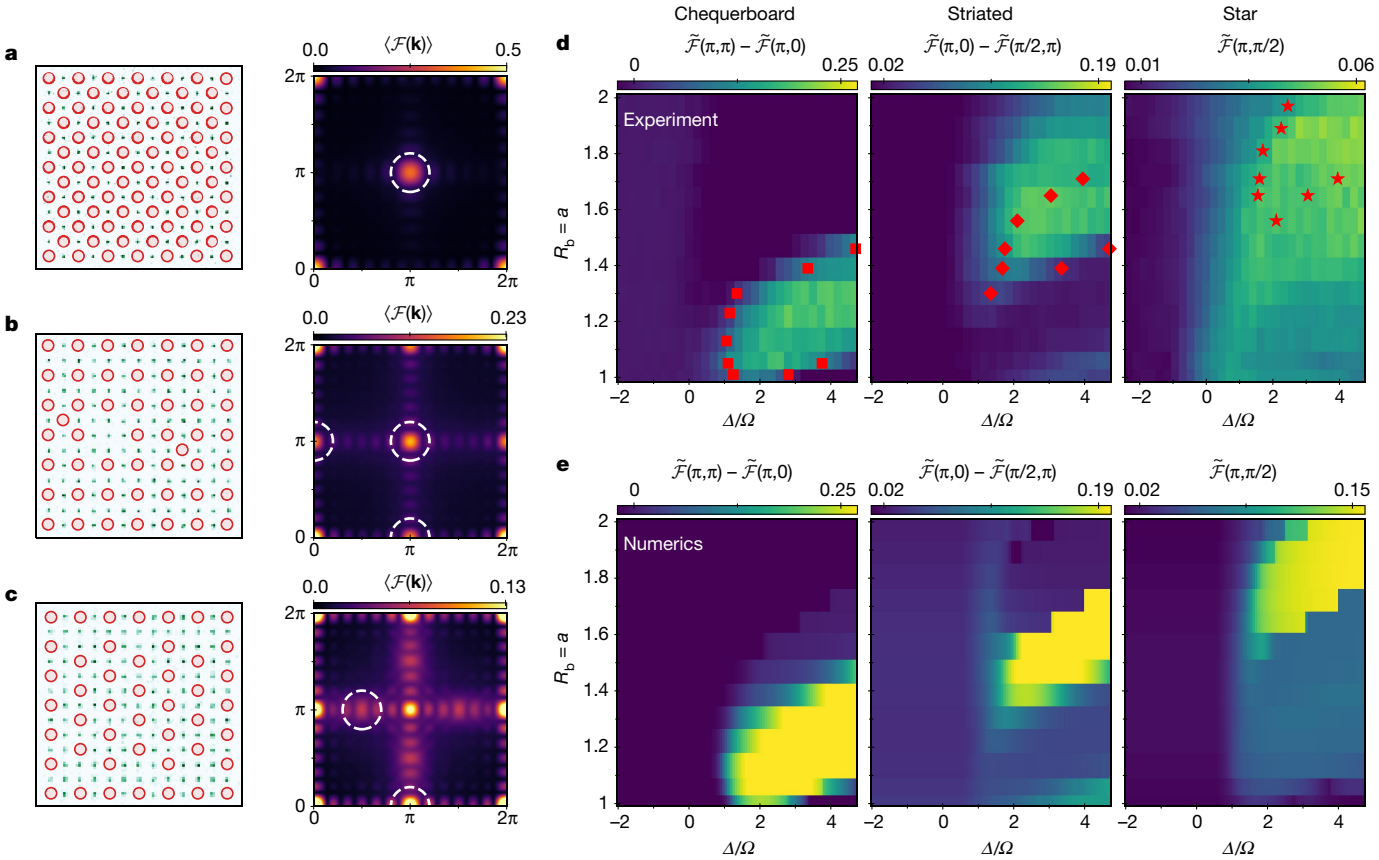

Fig. 4 | Phase diagram of the two-dimensional square lattice. a, Example fluorescence image of atoms in the chequerboard phase and the corresponding Fourier transform averaged over many experimental repetitions $\langle \mathcal{F}(\mathbf{k}) \rangle$, highlighting the peak at (π,π) (circled). **b**, Image of atoms in the striated phase and the corresponding $\langle \mathcal{F}(\mathbf{k}) \rangle$ highlighting peaks at (0,π), (π,0) and (π,π) (circled). **c**, Image of atoms in the star phase with corresponding Fourier peaks at (π/2,π) and (π,0) (circled), as well as at symmetric partners (π,π/2) and (0,π). **d**, The experimental phase diagram is constructed by measuring order parameters for each of the three phases for different values of the tunable blockade range R_b/a and detuning Δ/Ω. Red markers indicate the numerically calculated phase boundaries (see Methods). **e**, The order parameters evaluated numerically for the ground state using DMRG for a 9 × 9 array (see Methods). (Note different dimensionless colour scales used for the star phase comparison.)

Having identified the position of the critical point, we now extract the value of ν that optimizes data collapse (inset of Fig. 3d and Methods). The resulting $\nu = 0.62(4)$ rescales the experimental data to clearly fall on a single universal curve (Fig. 3d). This measurement is in good agreement with the value of $\nu = 0.629$ predicted for the quantum Ising universality class in (2 + 1) dimensions[14], and distinct from both the mean-field value[13] of $\nu = 1/2$ and the previously verified value in (1 + 1) dimensions[24] of $\nu = 1$ (also corresponding to the 2D classical Ising phase transition). The extracted critical exponent ν is consistent across different array sizes (Extended Data Fig. 8) and has an uncertainty dominated by the precision of our independent measurement of the location of the quantum critical point (see Methods). This demonstration of universal scaling constitutes a clear signature of quantum many-body behaviour, and highlights opportunities for quantitative studies of quantum critical phenomena.

Phase diagram of the square lattice

A rich variety of new phases has been recently predicted for the square lattice when Rydberg blockade is extended beyond nearest neighbours[14]. To map this phase diagram experimentally, we use the Fourier transform of single-shot measurement outcomes, $\mathcal{F}(\mathbf{k}) = |\sum_i \exp(i\mathbf{k} \cdot \mathbf{x}_i/a) n_i/N|$, which characterizes long-range order in our system. For instance, the chequerboard phase shows a prominent peak at $\mathbf{k} = (\pi,\pi)$, corresponding to the canonical antiferromagnetic order parameter: the staggered magnetization (Fig. 4a). We construct order parameters for all observed phases using the symmetrized Fourier transform $\tilde{\mathcal{F}}(k_1, k_2) = \langle \mathcal{F}(k_1, k_2) + \mathcal{F}(k_2, k_1) \rangle/2$, averaged over experimental repetitions, which takes into account the reflection symmetry in our system (see Methods).

When interaction strengths are increased such that next-nearest (diagonal) neighbour excitations are suppressed by Rydberg interactions ($R_b/a \gtrsim \sqrt{2}$), translational symmetry along the diagonal directions is also broken, leading to the appearance of a new striated phase (Fig. 4b). In this phase, Rydberg excitations are mostly located two sites apart and hence appear both on alternating rows and alternating columns. This ordering is immediately apparent through the observation of prominent peaks at $\mathbf{k} = (0,\pi)$, $(\pi,0)$ and (π,π) in the Fourier domain. As discussed and demonstrated below, quantum fluctuations, appearing as defects on single-shot images (Fig. 4b), have a key role in stabilizing this phase.

At even larger values of $R_b/a \gtrsim 1.7$, the star phase emerges, with Rydberg excitations placed every four sites along one direction and every two sites in the perpendicular direction. There are two possible orientations for the ordering of this phase, so Fourier peaks are observed at $\mathbf{k} = (\pi,0)$ and $(\pi/2,\pi)$, as well as at their symmetric partners $(0,\pi)$ and $(\pi,\pi/2)$ (Fig. 4c). In the thermodynamic limit, the star ordering corresponds to the lowest-energy classical configuration of Rydberg excitations on a square array with a density of 1/4.

We now systematically explore the phase diagram on 13 × 13 (169 atoms) arrays, with dimensions chosen to be simultaneously commensurate with chequerboard, striated and star orderings (see Methods). For each value of the blockade range R_b/a, we linearly sweep Δ (similar

to Fig. 3a but with a ramp-down time of 200 ns for Ω), stopping at evenly spaced endpoints to raster the full phase diagram. For every endpoint, we extract the order parameter corresponding to each many-body phase, and plot them separately to show their prominence in different regions of the phase diagram (Fig. 4d).

We compare our observations with numerical simulations of the ground state phase diagram using the density-matrix renormalization group (DMRG) on a smaller 9×9 array with open boundary conditions—the largest system size accessible with a similar phase diagram (Fig. 4e and red markers in Fig. 4d) (see Methods). We find excellent agreement in the extent of the chequerboard phase. For the striated and star phases, we also find good similarity between experiment and theory, although, owing to their larger unit cells and the existence of many degenerate configurations, these two phases are more sensitive to both edge effects and experimental imperfections. We emphasize that the numerical simulations evaluate the order parameter for the exact ground state of the system at each point, whereas the experiment quasi-adiabatically prepares these states via a dynamical process. These results establish the potential of programmable quantum simulators with tunable, long-range interactions for studying large quantum many-body systems that are challenging to access with state-of-the-art computational tools[40].

Quantum fluctuations in the striated phase

We now explore the nature of the striated phase. In contrast to the chequerboard and star phases, which can be understood from a dense-packing argument[14], this phase has no counterpart in the classical limit ($\Omega \to 0$) (see Methods). Striated ordering allows the atoms to lower their energy by partially aligning with the transverse field, favouring this phase at finite Ω. This can be seen by considering the 2×2 unit cell, within which one site has a large Rydberg excitation probability (designated the (0,0) sublattice) (Fig. 5a). Excitations on its nearest-neighbour (0,1) and (1,0) sublattices are suppressed owing to strong Rydberg blockade. The remaining atoms on the (1,1) sublattice have no nearest neighbours in the Rydberg state and experience a much weaker interaction from four next-nearest (diagonal) neighbours on the (0,0) sublattice, thus allowing the (1,1) atoms to lower their energy by forming a coherent superposition between ground and Rydberg states (Fig. 5b).

We experimentally study quantum fluctuations in this phase by observing the response of the system to short quenches (with quench times $t_q < 1/\Omega_q$). The dependence on the detuning Δ_q and laser phase ϕ_q of the quench (where $\Omega \to \Omega e^{i\phi q}$ in equation (1)) contains information about local correlations and coherence, which allows us to characterize the quantum states on the different sublattices. The quench resonance for each site is determined by the strong interactions with its nearest and next-nearest neighbours, resulting in a large difference between the (0,0) and (1,1) sublattices. Therefore, when one sublattice is resonantly driven, the other is effectively frozen on the short timescale t_q.

The nature of the striated phase is revealed using nine-particle operators to measure the state of an atom, conditioned on its local environment. Specifically, we evaluate the conditional Rydberg density $P^{(d)}$, defined as the excitation probability of an atom if all nearest neighbours are in $|g\rangle$ and exactly d next-nearest (diagonal) neighbours are in $|r\rangle$ (see Methods). For $d = 0$, we observe a dip in $P^{(0)}$ near the bare atom resonance (Fig. 5c), corresponding to resonant de-excitation of the (0,0) sublattice. Meanwhile, $P^{(3)}$ and $P^{(4)}$ have two separate peaks that correspond to resonant excitation of the (1,1) sublattice with $d = 3$ and $d = 4$ next-nearest neighbour excitations, respectively (Fig. 5c). Remarkably, we find that the quench response of both the (0,0) and (1,1) sublattices depends on the phase ϕ_q of the driving field during the quench (Fig. 5d, e). The measured visibilities, together with a simple mean-field model (see Methods), enable the estimation of unknown Bloch vector components on the two sublattices, yielding $\langle\sigma_x\rangle_{(0,0)} = -0.82(6)$, $\langle\sigma_y\rangle_{(0,0)} = 0.25(2)$, and $\langle\sigma_x\rangle_{(1,1)} = -0.46(4)$, $\langle\sigma_y\rangle_{(1,1)} = 0.01(1)$. We emphasize that accurate characterization requires the use of more sophisticated variational wavefunctions (based on, for example, tensor networks) and warrants further investigation. This approach can also be extended through techniques such as shadow tomography[41] and can be applied to probe the coherence properties of highly entangled quantum states of matter[42–44].

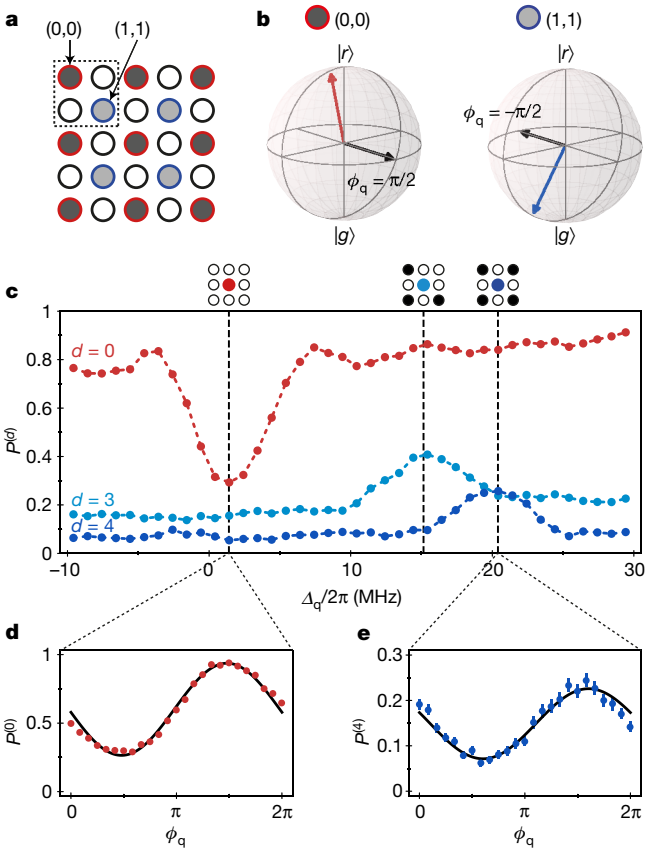

Fig. 5 | Probing correlations and coherence in the striated phase via quench dynamics. a, Unit cell of striated ordering (dashed box) with (0,0) and (1,1) sublattices outlined in red and blue, respectively. The fill shade on each site reflects the mean Rydberg excitation. **b**, The variational states for the (0,0) and (1,1) sublattices are illustrated on the Bloch sphere (see Methods). The black arrow illustrates the phase ϕ_q of Ω during the quench. **c**, Probability $P^{(d)}$ (where d is number of diagonal neighbour excitations) of an excitation, conditioned on observing no nearest-neighbour excitations, and zero (red), three (light blue) or four (dark blue) diagonal next-nearest neighbour excitations. $P^{(0)}$ is plotted for $\phi_q = \pi/2$, showing resonant de-excitation of the (0,0) sublattice near the bare-atom resonance (leftmost vertical line). $P^{(3)}$ and $P^{(4)}$ are plotted for $\phi_q = -\pi/2$, showing excitation peaks for the (1,1) sublattice at interaction shifts corresponding to three or four diagonal neighbours (two rightmost vertical lines). **d**, **e**, $P^{(0)}$ and $P^{(4)}$ vary with quench phase ϕ_q at their corresponding resonances ($\Delta_q/2\pi = 1.4$ and 20.4 MHz, respectively), demonstrating coherence on both the (0,0) and (1,1) sublattices. Solid line fits are used to extract Bloch vector components. Error bars represent one standard deviation.

Outlook

These experiments demonstrate that 2D Rydberg atom arrays constitute a powerful platform for programmable quantum simulations with hundreds of qubits. We expect that system size, quantum control fidelity and degree of programmability can all be increased considerably through technical improvements. In particular, array sizes and rearrangement fidelities, along with atomic-state readout, are currently limited by collisions with background gas particles, and can be

improved with an upgraded vacuum system[25] and increased photon collection efficiency. Quantum coherence can be enhanced by using higher-power Rydberg lasers and by encoding qubits in hyperfine ground states[19,28]. Tweezers with different atomic[25,30,45] and molecular[46,47] species can provide additional features and lead to new applications in both quantum simulations and metrology. Finally, rapidly switchable local control beams can be used to perform universal qubit operations in parallel across the system.

Our experiments realize several new quantum phases and provide insights into quantum phase transitions in 2D systems. These studies can be extended along several directions, including the exploration of non-equilibrium entanglement dynamics through rapid quenches across quantum phase transitions[48–50], the study of surface criticality in systems with sharp boundaries[51], the investigation of topological quantum states of matter on frustrated lattices[42–44], the simulation of lattice gauge theories[52,53] and the study of broader classes of spin models using hyperfine encoding[54]. Quantum information processing can also be explored with hardware-efficient methods for multi-qubit operations[28] and protocols for quantum error correction and fault-tolerant control[55]. Finally, our approach is well suited for efficient implementation of new algorithms for quantum optimization[56,57] and sampling[58], enabling experimental tests of their performance with system sizes exceeding several hundred qubits.

During the completion of this work, we became aware of related work demonstrating quantum simulations of 2D antiferromagnets with hundreds of Rydberg atoms[59].

Online content

Any methods, additional references, Nature Research reporting summaries, source data, extended data, supplementary information, acknowledgements, peer review information; details of author contributions and competing interests; and statements of data and code availability are available at https://doi.org/10.1038/s41586-021-03582-4.

1. Preskill, J. Quantum computing in the NISQ era and beyond. *Quantum* **2**, 79 (2018).
2. Zhang, J. et al. Observation of a many-body dynamical phase transition with a 53-qubit quantum simulator. *Nature* **551**, 601–604 (2017).
3. Gross, C. & Bloch, I. Quantum simulations with ultracold atoms in optical lattices. *Science* **357**, 995–1001 (2017).
4. Choi, J.-y. et al. Exploring the many-body localization transition in two dimensions. *Science* **352**, 1547–1552 (2016).
5. Mazurenko, A. et al. A cold-atom Fermi–Hubbard antiferromagnet. *Nature* **545**, 462–466 (2017).
6. Bernien, H. et al. Probing many-body dynamics on a 51-atom quantum simulator. *Nature* **551**, 579–584 (2017).
7. Neill, C. et al. Accurately computing electronic properties of a quantum ring. Preprint at https://arxiv.org/abs/2012.00921v2 (2021).
8. Wang, C. S. et al. Efficient multiphoton sampling of molecular vibronic spectra on a superconducting bosonic processor. *Phys. Rev. X* **10**, 021060 (2020).
9. Arute, F. et al. Quantum supremacy using a programmable superconducting processor. *Nature* **574**, 505–510 (2019).
10. Zhong, H.-S. et al. Quantum computational advantage using photons. *Science* **370**, 1460–1463 (2020).
11. Giovannetti, V., Lloyd, S. & Maccone, L. Advances in quantum metrology. *Nat. Photon.* **5**, 222–229 (2011).
12. Browaeys, A. & Lahaye, T. Many-body physics with individually controlled Rydberg atoms. *Nat. Phys.* **16**, 132–142 (2020).
13. Sachdev, S. *Quantum Phase Transitions* 2nd edn (Cambridge Univ. Press, 2011).
14. Samajdar, R., Ho, W. W., Pichler, H., Lukin, M. D. & Sachdev, S. Complex density wave orders and quantum phase transitions in a model of square-lattice Rydberg atom arrays. *Phys. Rev. Lett.* **124**, 103601 (2020).
15. Pagano, G. et al. Quantum approximate optimization of the long-range Ising model with a trapped-ion quantum simulator. *Proc. Natl Acad. Sci. USA* **117**, 25396–25401 (2020).
16. Friis, N. et al. Observation of entangled states of a fully controlled 20-qubit system. *Phys. Rev. X* **8**, 021012 (2018).
17. Harris, R. et al. Phase transitions in a programmable quantum spin glass simulator. *Science* **361**, 162–165 (2018).
18. Labuhn, H. et al. Tunable two-dimensional arrays of single Rydberg atoms for realizing quantum Ising models. *Nature* **534**, 667–670 (2016).
19. Morgado, M. & Whitlock, S. Quantum simulation and computing with Rydberg qubits. *AVS Quantum Sci.* **3**, 023501 (2021).
20. Lienhard, V. et al. Observing the space- and time-dependent growth of correlations in dynamically tuned synthetic Ising models with antiferromagnetic interactions. *Phys. Rev. X* **8**, 021070 (2018).
21. Guardado-Sanchez, E. et al. Probing the quench dynamics of antiferromagnetic correlations in a 2D quantum Ising spin system. *Phys. Rev. X* **8**, 021069 (2018).
22. Kim, H., Park, Y., Kim, K., Sim, H.-S. & Ahn, J. Detailed balance of thermalization dynamics in Rydberg-atom quantum simulators. *Phys. Rev. Lett.* **120**, 180502 (2018).
23. de Léséleuc, S. et al. Observation of a symmetry-protected topological phase of interacting bosons with Rydberg atoms. *Science* **365**, 775–780 (2019).
24. Keesling, A. et al. Quantum Kibble–Zurek mechanism and critical dynamics on a programmable Rydberg simulator. *Nature* **568**, 207–211 (2019).
25. Madjarov, I. S. et al. High-fidelity entanglement and detection of alkaline-earth Rydberg atoms. *Nat. Phys.* **16**, 857–861 (2020).
26. Omran, A. et al. Generation and manipulation of Schrödinger cat states in Rydberg atom arrays. *Science* **365**, 570–574 (2019).
27. Graham, T. M. et al. Rydberg mediated entanglement in a two-dimensional neutral atom qubit array. *Phys. Rev. Lett.* **123**, 230501 (2019).
28. Levine, H. et al. Parallel implementation of high-fidelity multiqubit gates with neutral atoms. *Phys. Rev. Lett.* **123**, 170503 (2019).
29. Madjarov, I. S. et al. An atomic-array optical clock with single-atom readout. *Phys. Rev. X* **9**, 041052 (2019).
30. Young, A. W. et al. Half-minute-scale atomic coherence and high relative stability in a tweezer clock. *Nature* **588**, 408–413 (2020).
31. Schymik, K.-N. et al. Enhanced atom-by-atom assembly of arbitrary tweezers arrays. *Phys. Rev. A* **102**, 063107 (2020).
32. Kumar, A., Wu, T.-Y., Giraldo, F. & Weiss, D. S. Sorting ultracold atoms in a three-dimensional optical lattice in a realization of Maxwell's demon. *Nature* **561**, 83–87 (2018).
33. Ohl de Mello, D. et al. Defect-free assembly of 2D clusters of more than 100 single-atom quantum systems. *Phys. Rev. Lett.* **122**, 203601 (2019).
34. Barredo, D., Lienhard, V., de Léséleuc, S., Lahaye, T. & Browaeys, A. Synthetic three-dimensional atomic structures assembled atom by atom. *Nature* **561**, 79–82 (2018).
35. Barredo, D., de Léséleuc, S., Lienhard, V., Lahaye, T. & Browaeys, A. An atom-by-atom assembler of defect-free arbitrary 2D atomic arrays. *Science* **354**, 1021–1023 (2016).
36. Jaksch, D. et al. Fast quantum gates for neutral atoms. *Phys. Rev. Lett.* **85**, 2208 (2000).
37. Lukin, M. D. et al. Dipole blockade and quantum information processing in mesoscopic atomic ensembles. *Phys. Rev. Lett.* **87**, 037901 (2001).
38. Gardas, B., Dziarmaga, J., Zurek, W. H. & Zwolak, M. Defects in quantum computers. *Sci. Rep.* **8**, 4539 (2018).
39. Zurek, W. H., Dorner, U. & Zoller, P. Dynamics of a quantum phase transition. *Phys. Rev. Lett.* **95**, 105701 (2005).
40. Felser, T., Notarnicola, S. & Montangero, S. Efficient tensor network ansatz for high-dimensional quantum many-body problems. *Phys. Rev. Lett.* **126**, 170603 (2021).
41. Huang, H.-Y., Kueng, R. & Preskill, J. Predicting many properties of a quantum system from very few measurements. *Nat. Phys.* **16**, 1050–1057 (2020).
42. Verresen, R., Lukin, M. D. & Vishwanath, A. Prediction of toric code topological order from Rydberg blockade. Preprint at https://arxiv.org/abs/2011.12310 (2020).
43. Samajdar, R., Ho, W. W., Pichler, H., Lukin, M. D. & Sachdev, S. Quantum phases of Rydberg atoms on a kagome lattice. *Proc. Natl Acad. Sci. USA* **118**, e2015785118 (2021).
44. Semeghini, G. et al. Probing topological spin liquids on a programmable quantum simulator. Preprint at https://arxiv.org/abs/2104.04119 (2021).
45. Saskin, S., Wilson, J. T., Grinkemeyer, B. & Thompson, J. D. Narrow-line cooling and imaging of ytterbium atoms in an optical tweezer array. *Phys. Rev. Lett.* **122**, 143002 (2019).
46. Anderegg, L. et al. An optical tweezer array of ultracold molecules. *Science* **365**, 1156–1158 (2019).
47. Liu, L. R. et al. Building one molecule from a reservoir of two atoms. *Science* **360**, 900–903 (2018).
48. Turner, C. J., Michailidis, A. A., Abanin, D. A., Serbyn, M. & Papić, Z. Weak ergodicity breaking from quantum many-body scars. *Nat. Phys.* **14**, 745–749 (2018).
49. Surace, F. M. et al. Lattice gauge theories and string dynamics in Rydberg atom quantum simulators. *Phys. Rev. X* **10**, 021041 (2020).
50. Bluvstein, D. et al. Controlling quantum many-body dynamics in driven Rydberg atom arrays. *Science* **371**, 1355–1359 (2021).
51. Diehl, H. W. The theory of boundary critical phenomena. *Int. J. Mod. Phys. B* **11**, 3503–3523 (1997).
52. Bañuls, M. C. et al. Simulating lattice gauge theories within quantum technologies. *Eur. Phys. J. D* **74**, 165 (2020).
53. Notarnicola, S., Collura, M. & Montangero, S. Real-time-dynamics quantum simulation of (1 + 1)-dimensional lattice QED with Rydberg atoms. *Phys. Rev. Research* **2**, 013288 (2020).
54. Weimer, H., Müller, M., Lesanovsky, I., Zoller, P. & Büchler, H. P. A Rydberg quantum simulator. *Nat. Phys.* **6**, 382–388 (2010).
55. Auger, J. M., Bergamini, S. & Browne, D. E. Blueprint for fault-tolerant quantum computation with Rydberg atoms. *Phys. Rev. A* **96**, 052320 (2017).
56. Farhi, E., Goldstone, J. & Gutmann, S. A quantum approximate optimization algorithm. Preprint at https://arxiv.org/abs/1411.4028 (2014).
57. Zhou, L., Wang, S.-T., Choi, S., Pichler, H. & Lukin, M. D. Quantum approximate optimization algorithm: performance, mechanism, and implementation on near-term devices. *Phys. Rev. X* **10**, 021067 (2020).
58. Wild, D. S., Sels, D., Pichler, H. & Lukin, M. D. Quantum sampling algorithms for near-term devices. Preprint at https://arxiv.org/abs/2005.14059 (2020).
59. Scholl, P. et al. Programmable quantum simulation of 2D antiferromagnets with hundreds of Rydberg atoms. *Nature* https://doi.org/10.1038/s41586-021-03585-1 (2021).

Methods

2D optical tweezer array

Our 2D tweezer array is generated by a free-running 810-nm Ti:sapphire laser (M Squared, 18-W pump). The laser illuminates a phase-control spatial light modulator (Hamamatsu X13138-02), which imprints a computer-generated hologram on the wavefront of the laser field. The phase hologram is calculated using the phase-fixed weighted Gerchberg–Saxton (WGS) algorithm[60] to produce an arbitrary arrangement of tweezer spots after propagating to the focus of a microscope objective (Mitutoyo: 3.5 mm glass thickness corrected, 50×, NA = 0.5). Using this method, we can create tweezer arrays with roughly 1,000 individual tweezers (Extended Data Fig. 1). When calculating the phase hologram, we improve trap homogeneity by pre-compensating for the variation in diffraction efficiency across the tweezer array (roughly given by $\mathrm{sinc}^2(\frac{\pi}{2}(\theta_{\mathrm{trap}}/\theta_{\mathrm{max}}))$ where θ denotes the deflection angle from zeroth order).

We also use the phase control of our SLM to correct for optical aberrations on tweezers within the experimentally used field of view at the plane of atoms (Extended Data Fig. 2). Aberrations reduce the peak intensity of focal spots (characterized by the Strehl ratio) and correspondingly reduce the light shift of our tweezers on the atoms. By measuring these light shifts as we apply a wavefront correction to the SLM, parametrized by several low-order Zernike polynomials with varying amplitudes, we quantify and correct for different aberrations in our optical system (Extended Data Fig. 2a). Using this method, we compensate for 70 milliwaves of aberrations, observe a total increase of 18% in our trap intensity (Extended Data Fig. 2c) and measure a corresponding reduction in the range of trap frequencies (Extended Data Fig. 2d). Aberration correction additionally allows us to place tweezers closer together (minimum separation 3 μm) to reach larger blockade ranges R_b/a.

Tweezers in the array have waists ~900 nm, trap depths of ~$2\pi \times 17$ MHz and radial trap frequencies of ~$2\pi \times 80$ kHz. In each experimental cycle, the tweezers are loaded from a magneto-optical trap with uniform loading probabilities of 50–60% after 50–100 ms loading time.

Atom rearrangement

Atoms are rearranged using an additional set of dynamically moving tweezers, which are overlaid on top of the SLM tweezer array. These movable tweezers are generated by a separate 809-nm laser source (DBR from Photodigm and tapered amplifier from MOGLabs) and are steered with a pair of independently controlled crossed acousto-optic deflectors (AODs) (AA Opto Electronic DTSX-400). Both AODs are driven by an arbitrary waveform which is generated in real time using our home-built waveform generation software and an arbitrary waveform generator (AWG) (M4i.6631-x8, Spectrum Instrumentation). Dynamically changing the RF frequency allows for continuous steering of beam positions, and multi-frequency waveforms allow for multiple moving tweezers to be created in parallel[61].

Although many 2D sorting protocols have been described previously[31,33,35,62,63], we implement a new protocol designed to leverage parallel movement of multiple atoms simultaneously. More specifically, we create a row of moving traps which scans upwards along the SLM tweezer array to move one atom within each column up in parallel. This is accomplished by scanning a single frequency component on the vertical AOD to move from the bottom to the top of the SLM array, during which individual frequency components are turned on and off within the horizontal AOD to create and remove tweezers at the corresponding columns. This protocol is designed for SLM tweezer arrays in which traps are grouped into columns and rows. Although this does constrain the possible geometries, most lattice geometries of interest can still be defined on a subset of points along fixed columns and rows.

Rearrangement algorithm

Here we detail the rearrangement algorithm, which is illustrated in Extended Data Fig. 3. It operates on an underlying rectangular grid of rows and columns, where the SLM traps correspond to vertices of the grid. We pre-program a set of 'target traps' that we aim to fill.

Pre-sorting. We begin by ensuring that each column contains a sufficient number of atoms to fill the target traps in that column. In each experimental cycle, owing to the random loading throughout the array, some columns may contain excess atoms while other columns may lack a sufficient number of atoms. Accordingly, we apply a 'pre-sorting' procedure in which we move atoms between columns. To fill a deficient column j, we take atoms from whichever side of j has a larger surplus. We identify which atoms to take by finding the nearest atoms from the surplus side that are in rows for which column j has an empty trap. We then perform parallel horizontal sorting to move these atoms into the empty traps of j (not all surplus atoms need to be from the same source column).

If the one-side surplus is insufficient to fill column j, then we move as many surplus atoms as possible from this one side and leave j deficient. We then proceed to the next deficient column, and cycle through until all columns have sufficient atoms. In typical randomly loaded arrays, this process takes a small number of atom moves compared with the total number of moves needed for sorting. This specific algorithm can fail to properly distribute atoms between columns owing to lack of available atoms, but these failures are rare and do not limit the experimental capabilities.

Ejection. After pre-sorting, we eject excess atoms in parallel by scanning the vertical AOD frequency downward, beginning at a row in which we want to pick up an atom, and ending below the bottom row of the array. In each downward scan, we eject a single atom from each column containing excess atoms; we repeat this process until all excess atoms are ejected.

Parallel sorting within columns. After pre-sorting and ejection, each column has the correct number of atoms to fill all of its target traps by moving atoms up/down within the column. We now proceed to shuffle the ith-highest loaded atoms to the ith-highest target traps. As the atoms cannot move through each other, in a single vertical scan atoms are moved as close as possible to their target locations, reaching their targets unless they are blocked by another atom. We repeat upward/downward scans until all atoms reach their target locations.

Rearrangement parameters and results

When using moving tweezers to pick up and drop off atoms in the SLM traps, the moving tweezers ramp on/off over 15 μs while positioned to overlap with the corresponding SLM trap. The moving tweezers are approximately twice as deep as the static traps, and move atoms between SLM traps with a speed of 75 μm ms^{-1}. Typical rearrangement protocols take a total of 50–100 ms to implement in practice, depending on the size of the target array and the random initial loading. Alignment of the AOD traps onto the SLM array is pre-calibrated by measuring both trap arrays on a monitor CMOS camera and tuning the AOD frequencies to match positions with traps from the SLM array.

A single round of rearrangement results in typical filling fractions of ~98.5% across all target traps in the system. This is limited primarily by the finite vacuum-limited lifetime (~10 s) and the duration of the rearrangment procedure. To increase filling fractions, we perform a second round of rearrangement (having skipped ejection in the first round to keep excess atoms for the second round). Because the second round of rearrangement only needs to correct for a small number of defects, it requires far fewer moves and can be performed more quickly, resulting in less background loss. With this approach, we achieve filling fractions of ~99.2% over more than 200 sites, with a total experimental cycle time of 400 ms.

Rydberg laser system

Our Rydberg laser system is an upgraded version of a previous set-up[26]. The 420-nm laser is a frequency-doubled Ti:sapphire laser (M Squared,

15-W pump). We stabilize the laser frequency by locking the fundamental to an upgraded ultra-low-expansion (ULE) reference cavity (notched cylinder design, Stable Laser Systems), with finesse $\mathcal{F} = 30{,}000$ at 840 nm. The 1,013-nm laser source is an external-cavity diode laser (Toptica DL Pro), which is locked to the same reference cavity ($\mathcal{F} = 50{,}000$ at 1,013 nm). To suppress high-frequency phase noise from this diode laser, we use the transmitted light through the cavity, which is filtered by the narrow cavity transmission spectrum (30 kHz linewidth)[64]. This filtered light is used to injection-lock another laser diode, whose output is subsequently amplified to 10 W by a fibre amplifier (Azur Light Systems).

Using beam shaping optics to homogeneously illuminate the atom array with both Rydberg lasers, we achieve single-photon Rabi frequencies of $(\Omega_{420}, \Omega_{1,013}) = 2\pi \times (160, 50)$ MHz. We operate with an intermediate state detuning $\delta = 2\pi \times 1$ GHz, resulting in two-photon Rabi frequency $\Omega = \Omega_{420}\Omega_{1,013}/2\delta \approx 2\pi \times 4$ MHz. Small inhomogeneities in the Rydberg beams result in Rabi frequency variations of ~2% RMS and ~6% peak-to-peak across the array. With these conditions, we estimate an off-resonant scattering rate of 1/(20 μs) for atoms in $|g\rangle$ and 1/(150 μs) for atoms in $|r\rangle$ at peak power.

Rydberg beam shaping

We illuminate our 2D atom array with counter-propagating Rydberg laser beams from each side. Instead of using elliptical Gaussian beams, we shape both Rydberg excitation beams into one-dimensional top-hats (light sheets) to homogeneously illuminate the plane of atoms (Extended Data Fig. 4). To ensure homogeneous illumination over the entire array, we define our target field profile in the plane of the atoms with both uniform amplitude cross-section and flat phase profile. Using a single phase-only SLM in the Fourier plane to control both phase and amplitude in the image plane is inherently limited in efficiency; therefore, in practice, we compromise between optimizing hologram efficiency and beam homogeneity. We generate these holograms using the conjugate gradient minimization algorithm (Extended Data Fig. 4c)[65]. In all experiments in this work, we use 1D top-hat beams with a flat-width of 105 μm and a perpendicular Gaussian width of 25 μm. The conversion efficiencies into the top-hat modes are 30% for 420 nm and 38% for 1,013 nm.

Since holographic beam shaping relies on the intricate interplay of different high spatial frequency components in the light field, it is extremely sensitive to optical aberrations. We correct for all aberrations up to the window of our vacuum chamber by measuring the amplitude and phase of the electric field as it propagates through the optical beampath (Extended Data Fig. 4a, b)[66]. We do so by picking off a small portion of the Rydberg beam and observing it on a camera with small pixel size and with sensor cover removed for high-fidelity beam characterization (Imaging Source DMM 27UP031-ML). In this way, we reduce the wavefront error in our beam down to $\lambda/100$, and also use the measured field profile as the starting guess in our hologram generation algorithm (Extended Data Fig. 4a, b). Furthermore, by imaging the top-hat beams we also correct for remaining inhomogeneities by updating the input of our optimization algorithm (Extended Data Fig. 4e, f). Owing to aberrations and imperfections of the vacuum windows, we observe slightly larger intensity variations on the atoms than expected (~3% RMS, ~10% peak-to-peak).

Rydberg pulses

After initializing our atoms in the ground state $|g\rangle$, the tweezer traps are turned off for a short time (<5 μs) during which we apply a Rydberg pulse. The pulse consists of a time-dependent Rabi frequency $\Omega(t)$, time-dependent detuning $\Delta(t)$, and a relative instantaneous phase $\phi(t)$. This is implemented by controlling the amplitude, frequency and phase of the 420-nm laser using a tandem acousto-optical modulator system, similar to what is described previously[26].

Quasi-adiabatic sweeps. To prepare many-body ground states with high fidelity, we use an optimized quasi-adiabatic pulse shape (Fig. 2a). The coupling $\Omega(t)$ is initially ramped on linearly at large fixed negative detuning, held constant during the detuning sweep $\Delta(t)$ and finally ramped down linearly at large fixed positive detuning. The detuning sweep consists of a cubic spline interpolation between five points: initial detuning, final detuning, an inflection point where the slope reaches a minimum, and two additional points that define the duration of the slow part of the sweep. The sweep used for finding perfect chequerboard ground-state probabilities (Fig. 2e) was obtained by optimizing the parameters of the spline cubic sweep to maximize the correlation length on a 12 × 12 (144 atoms) array. The sweep used in detection of the star and striated phases was optimized based on maximizing their respective order parameters. In particular, the inflection point was chosen to be near the position of the minimum gap in these sweeps in order to maximize adiabaticity.

Linear sweeps. To probe the phase transition into the chequerboard phase (Fig. 3), we use variable-endpoint linear detuning sweeps in which Ω is abruptly turned off after reaching the endpoint. This ensures that projective readout happens immediately after the end of the linear sweep instead of allowing time for further dynamics, and is essential for keeping the system within the quantum Kibble–Zurek regime. Linear sweeps are done from $\Delta = -16$ MHz to 14 MHz ($\Delta/\Omega = -3.7$ to 3.3) at sweep rates $s = 15, 21, 30, 42, 60, 85$ and 120 MHz μs^{-1}. Data for locating the quantum critical point (Extended Data Fig. 7a) are taken from the slowest of these sweeps ($s = 15$ MHz μs^{-1}) to remain as close as possible to the ground state. For mapping out the 2D phase diagram (Fig. 4), we use the same variable-endpoint linear sweeps at fixed sweep rate $s = 12$ MHz μs^{-1}, except that Ω is ramped down over 200 ns after reaching the endpoint.

State detection

At the end of the Rydberg pulse, we detect the state of atoms by whether or not they are recaptured in our optical tweezers. Atoms in $|g\rangle$ are recaptured and detected with fidelity 99%, limited by the finite temperature of the atoms and collisions with background gas particles in the vacuum chamber.

Atoms excited to the Rydberg state are detected as a loss signal due to the repulsive potential of the optical tweezers on $|r\rangle$. However, the finite Rydberg state lifetime[67] (~80 μs for $70S_{1/2}$) leads to a probability of ~15% for $|r\rangle$ atoms to decay to $|g\rangle$ and be recaptured by the optical tweezers. In our previous work[26], we increased tweezer trap depths immediately following the Rydberg pulse to enhance the loss signal for atoms in $|r\rangle$. In 2D, this approach is less effective, because atoms that drift away from their initial traps can still be recaptured in a large 3D trapping structure created by out-of-plane interference of tweezers.

Following an approach similar to what has been previously demonstrated[27], we increase the Rydberg detection fidelity using a strong microwave pulse to enhance the loss of atoms in $|r\rangle$ while leaving atoms in $|g\rangle$ unaffected. The microwave source (Stanford Research Systems SG384) is frequency-tripled to 6.9 GHz and amplified to 3 W (Minicircuits, ZVE-3W-183+). The microwave pulse, containing both 6.9 GHz and harmonics, is applied on the atoms using a microwave horn for 100 ns. When applying a Rydberg π-pulse immediately followed by the microwave pulse, we observe loss probabilities of 98.6(4)%. Since this measurement includes error in the π-pulse as well as detection errors, we apply a second Rydberg π-pulse after the microwave pulse, which transfers most of the remaining ground state population into the Rydberg state. In this configuration, we observe 99.1(4)% loss probability, which is our best estimate for our Rydberg detection fidelity (Extended Data Fig. 5). We find that the loss signal is enhanced by the presence of both microwave fundamental and harmonic frequencies.

Limits on ground-state preparation fidelity

Figure 2e shows an exponential scaling of ~0.97^N for the probability of preparing perfect chequerboard order versus system size. In this section, we provide an estimated accounting of possible contributions to the imperfect preparation of the ground state. We measure a ~1% detection infidelity for both the ground and Rydberg states, and therefore attribute the remaining ~2% of the errors to imperfect preparation of the many-body ground state of the system.

The dominant source of error for atoms in the ground state is scattering from the intermediate state caused by the 420-nm laser, with a rate of 1/(20 μs). The combination of Rydberg state spontaneous decay rate of 1/(375 μs), intermediate state scattering rate of 1/(150 μs) due to the 1,013-nm laser, and blackbody-induced decay at a rate of 1/(250 μs) gives a total decay rate of 1/(80 μs) for atoms in the Rydberg state. Although it is challenging to model how these errors contribute to the many-body state preparation, a simple estimate yields an error probability in excess of 10% per atom during a 2–3-μs sweep, much larger than the observed infidelity. These considerations indicate that some degree of error resilience is present in the many-body dynamics. This intriguing observation warrants further investigations.

Coarse-grained local staggered magnetization

We define the coarse-grained local staggered magnetization for a site i with column and row indices a and b, respectively, as:

$$m_i = \frac{(-1)^{a+b}}{N_i} \sum_{\langle j,i\rangle} (n_i - n_j)$$

where j is summed over nearest neighbours of site i and N_i is the number of such nearest neighbours (4 in the bulk, 3 along the edges or 2 on the corners). The value of m_i ranges from −1 to 1, with the extremal values corresponding to the two possible perfect antiferromagnetic orderings locally on site i and its nearest neighbours (Extended Data Fig. 6a, b). The two-site correlation function for m_i can then be defined as an average over experiment repetitions $G_m^{(2)}(k,l) = \frac{1}{N_{(k,l)}} \sum_{i,j} (\langle m_i m_j\rangle - \langle m_i\rangle\langle m_j\rangle)$, where the sum is over all pairs of sites i,j separated by a relative lattice distance of $\mathbf{x} = (k,l)$ sites and normalized by the number of such pairs $N_{(k,l)}$ (Extended Data Fig. 6c). We obtain the correlation length ξ_R by fitting an exponential decay to the radially averaged $G_m^{(2)}(k,l)$ (Extended Data Fig. 6d). The coarse-grained local staggered magnetization m_i is defined such that the corresponding $G_m^{(2)}(k,l)$ is isotropic (Extended Data Fig. 6c), which makes for natural radial averaging. This radial average captures correlations across the entire array better than purely horizontal or vertical correlation lengths ξ_H and ξ_V, which are more sensitive to edge effects.

Determination of the quantum critical point

To accurately determine the location of the quantum critical point Δ_c for the transition into the chequerboard phase, we measure mean Rydberg excitation $\langle n\rangle$ versus detuning Δ for a slow linear sweep with sweep rate $s = 15\ \mathrm{MHz\,\mu s^{-1}}$ (Extended Data Fig. 7a). To smooth the measured curve, we fit a polynomial for $\langle n\rangle$ versus Δ/Ω and take its numerical derivative to identify the peak of the susceptibility χ as the critical point[13] (Extended Data Fig. 7b).

Small oscillations in $\langle n\rangle$ result from the linear sweep not being perfectly adiabatic. To minimize the effect of this on our fitting, we use the lowest-degree polynomial (cubic) whose derivative has a peak, and choose a fit window in which the reduced chi-squared metric indicates a good fit. Several fit windows around $\Delta/\Omega = 0$ to 2 give good cubic fits, and we average results from each of these windows to obtain $\Delta_c/\Omega = 1.12(4)$.

We also numerically extract the critical point for a system with numerically tractable dimensions of 10 × 10. Using the density-matrix renormalization group (DMRG) algorithm, we evaluate $\langle n\rangle$ as a function of Δ and then take the derivative to obtain a peak of the susceptibility at $\Delta_c/\Omega = 1.18$ (Extended Data Fig. 7d, e). To corroborate the validity of our experimental fitting procedure, we also fit cubic polynomials to the DMRG data and find that the extracted critical point is close to the exact numerical value (Extended Data Fig. 7e). This numerical estimate of the critical point for a 10 × 10 array is consistent with the experimental result on a larger 16 × 16 array. Moreover, our experiments on arrays of different sizes show that Δ_c/Ω does not vary significantly between 12 × 12, 14 × 14 and 16 × 16 arrays (Extended Data Fig. 8b).

Data collapse for universal scaling

Optimizing the universal collapse of rescaled correlation length $\tilde{\xi}$ versus rescaled detuning $\tilde{\Delta}$ requires defining a measure of the distance between rescaled curves for different sweep rates s_i. Given $\tilde{\xi}_j^{(i)}$ and $\tilde{\Delta}_j^{(i)}$, where the index i corresponds to sweep rate s_i and j labels sequential data points along a given curve, we define a distance[68]

$$D = \sqrt{\frac{1}{N} \sum_i \sum_{i' \neq i} \sum_j |\tilde{\xi}_j^{(i')} - f^{(i)}(\tilde{\Delta}_j^{(i')})|^2}\,. \tag{4}$$

The function $f^{(i)}(\tilde{\Delta})$ is the linear interpolation of $\tilde{\xi}_j^{(i)}$ versus $\tilde{\Delta}_j^{(i)}$, while N is the total number of terms in the three nested sums. The sum over j only includes points that fall within the domain of overlap of all datasets, avoiding the problem of linear interpolation beyond the domain of any single dataset. Defined in this way, the collapse distance D measures all possible permutations of how far each rescaled correlation growth curve is from curves corresponding to other sweep rates.

Applied to our experimental data, D is a function of both the location of the critical point Δ_c and the critical exponent ν (Extended Data Fig. 8a). Using the independently measured $\Delta_c/\Omega = 1.12(4)$, we obtain $\nu = 0.62(4)$ for optimal data collapse and illustrate in particular the better collapse for this value than for other values of ν (Extended Data Fig. 8c–e). The quoted uncertainty is dominated by the corresponding uncertainty of the extracted Δ_c/Ω, rather than by the precision of finding the minimum of D for a given Δ_c/Ω. Note that in realistic systems sweeps across the phase transitions result in highly non-thermal states, which are challenging to describe within a simple framework[24]. As compared with methods used previously in a 1D system[24], the present approach is robust with respect to additional dynamics after crossing the critical point. Our experiments give consistent values of Δ_c/Ω and ν for systems of size 12 × 12, 14 × 14 and 16 × 16 (Extended Data Fig. 8b), suggesting that boundary effects do not significantly impact our results. However, the presence of sharp boundaries in our system offers the opportunity to study surface criticality[51], which in our system has a critical exponent[69] that is distinctly different from the bulk value $\nu = 0.629$.

Order parameters for many-body phases

We construct order parameters to identify each phase using the Fourier transform to quantify the amplitude of the observed density-wave ordering. We define the symmetrized Fourier transform $\tilde{\mathcal{F}}(k_1,k_2) = \langle \mathcal{F}(k_1,k_2) + \mathcal{F}(k_2,k_1)\rangle/2$ to take into account the C_4 rotation symmetry between possible ground-state orderings for some phases. For the star phase, the Fourier amplitude $\tilde{\mathcal{F}}(\pi,\pi/2)$ is a good order parameter because ordering at $\mathbf{k} = (\pi,\pi/2)$ is unique to this phase. The striated phase, on the other hand, shares its Fourier peaks at $\mathbf{k} = (\pi,0)$ and $(0,\pi)$ with the star phase, and its peak at $\mathbf{k} = (\pi,\pi)$ with the chequerboard phase; hence, none of these peaks alone can serve as an order parameter. We therefore construct an order parameter for the striated phase to be $\tilde{\mathcal{F}}(0,\pi) - \tilde{\mathcal{F}}(\pi/2,\pi)$, which is non-zero in the striated phase and zero in both chequerboard and star. Similarly, the chequerboard shares its $\mathbf{k} = (\pi,\pi)$ peak with the striated phase, so we construct $\tilde{\mathcal{F}}(\pi,\pi) - \tilde{\mathcal{F}}(0,\pi)$ as an order parameter that is zero in the striated phase and non-zero only in chequerboard.

Numerical simulations using DMRG

We numerically compute the many-body ground states at different points in the $(\Delta/\Omega, R_b/a)$ phase diagram using the DMRG algorithm[70,71], which operates in the space of the so-called matrix product state ansätze. Although originally developed for 1D systems, DMRG can also be extended to two dimensions by representing the 2D system as a winding 1D lattice[72], albeit with long-range interactions. A major limitation to 2D DMRG is that the number of states required to faithfully represent the ground-state wavefunction has to be increased exponentially with the width of the system in order to maintain a constant accuracy. For our calculations, we use a maximum bond dimension of 1,600, which allows us to accurately simulate 10×10 square arrays[14]. We also impose open boundary conditions in both directions and truncate the van der Waals interactions so as to retain up to third-nearest-neighbour couplings. The numerical convergence criterion is set by the truncation error, and the system is regarded to be well-converged to its true ground state once this error drops below a threshold of 10^{-7}. In practice, this was typically found to be achieved after $\mathcal{O}(10^2)$ successive sweeps.

Since the dimensions of the systems studied in Fig. 4, 13×13 (experimentally) and 9×9 (numerically), are both of the form $(4n+1) \times (4n+1)$, the two phase diagrams are expected to be similar. In particular, both these system sizes are compatible with the commensurate ordering patterns of the crystalline phases observed in this work, and can host all three phases (at the appropriate R_b/a) with the same boundary conditions. Likewise, for extraction of the QCP, we use a 10×10 array as it is the largest numerically accessible square lattice comparable to the 16×16 array used in our study of the quantum phase transition.

Mean-field wavefunction for the striated phase

To understand the origin of the striated phase, it is instructive to start from a simplified model in which we assume that nearest-neighbour sites are perfectly blockaded. Since we always work in a regime where $R_b/a > 1$, this model should also capture the essential physics of the full Rydberg Hamiltonian.

In the classical limit of $\Omega = 0$, the perfect chequerboard state has an energy per site of $-\Delta/2 + V(\sqrt{2}\,a) + V(2a)$, with $V(x)$ being the interaction between sites at a distance x, whereas the corresponding energy for the star-ordered state is $-\Delta/4$ (neglecting interactions for $x > 2a$). Accordingly, there is a phase transition between the chequerboard and star phases when $\Delta = 4[V(\sqrt{2}\,a) + V(2a)]$. On the other hand, for the same density of Rydberg excitations, the striated phase has a classical energy per site of $-\Delta/4 + V(2a)/2$, which is always greater than that of the star phase; hence, striated ordering never appears in the classical limit.

At finite Ω, however, the striated phase emerges owing to a competition between the third-nearest-neighbour interactions and the second-order energy shift upon dressing a ground state atom off-resonantly with the Rydberg state. We can thus model the ground state of the striated phase as a product state, where (approximately) 1/2 of the atoms are in the ground state, 1/4 of the atoms are in the Rydberg state and the remaining 1/4 are in the ground state with a weak coherent admixture of the Rydberg state. A general mean-field ansatz for a many-body wavefunction of this form is given by

$$|\Psi_{\mathrm{str}}(a_1, a_2)\rangle = \bigotimes_{\mathbf{i}\in A_1} (\cos a_1 |g\rangle_{\mathbf{i}} + \sin a_1 |r\rangle_{\mathbf{i}}) \bigotimes_{\mathbf{i}\in A_2} (\cos a_2 |g\rangle_{\mathbf{i}} + \sin a_2 |r\rangle_{\mathbf{i}}) \bigotimes_{\mathbf{j}\in B} |g\rangle_{\mathbf{j}}, \quad (5)$$

where A_1 and A_2 represent the two sublattices of the (bipartite) A sublattice, and $a_{1,2}$ are variational parameters. If $a_1 = a_2$, then our trial wavefunction simply represents a chequerboard state, but if $a_1 \neq a_2$, this state is not of the chequerboard type and leads to the striated phase.

Based on this ansatz, we can now explicitly see how the striated phase may become energetically favourable in the presence of a non-zero Ω. Consider the atoms on the partially excited sublattice to be in the superposition $|g\rangle + [\Omega/\{4V(\sqrt{2}\,a) - \Delta\}]|r\rangle$; this describes the state of the atoms on the (1,1) sublattice in the notation of Fig. 5. The net energy per site of the system is then

$$-\frac{\Delta}{4} + \frac{V(2a)}{2} - \frac{\Omega^2}{4\,(4V(\sqrt{2}\,a) - \Delta)} + \frac{\Omega^2\, V(\sqrt{2}\,a)}{2\,(4V(\sqrt{2}\,a) - \Delta)^2}$$

where the third and fourth terms are the second-order energy shift and mean-field interaction shift, respectively. From this expression, we observe that if the energy gained from the dressing (these last two terms) is larger than $V(2a)/2$, then the striated phase prevails over the star phase.

Dynamical probe of the striated phase

We prepare striated ordering using an optimized cubic spline sweep along $R_b/a = 1.47$, ending at $\Delta/\Omega = 2.35$. Immediately after this sweep, the system is quenched to detuning Δ_q and relative laser phase ϕ_q. We quench at a lower Rabi frequency $\Omega_q = \Omega/4 \approx 2\pi \times 1$ MHz to improve the resolution of this interaction spectroscopy. For the chosen lattice spacing, the interaction energy between diagonal excitations is $2\pi \times 5.3$ MHz. The reference phase for the atoms $\phi = 0$ is set by the instantaneous phase of the Rydberg coupling laser at the end of the sweep into striated ordering. In the Bloch sphere picture, $\phi = 0$ corresponds to the $+x$ axis, so the wavefunctions on (0,0) and (1,1) sublattices correspond to vectors pointing mostly up or mostly down with a small projection of each along the $+x$ axis. In the same Bloch sphere picture, quenching at $\phi_q = \pi/2$ or $-\pi/2$ corresponds to rotations around the $+y$ or $-y$ axes (Fig. 5b).

To resolve the local response of the system, we use high-order correlators which are extracted from single-shot site-resolved readout. In particular, we define an operator $\hat{\mathcal{O}}_i^{(d)}$ on the eight atoms surrounding site i. This operator projects the neighbouring atoms into configurations in which all four nearest atoms are in $|g\rangle$ and exactly d of the diagonal neighbours are in $|r\rangle$. Specifically, the operator $\hat{\mathcal{O}}_i^{(d)}$ decomposes into a projector $\hat{A}_i$ on the four nearest neighbouring atoms and $\hat{B}_i^{(d)}$ on the four diagonal neighbours, according to $\hat{\mathcal{O}}_i^{(d)} = \hat{A}_i \hat{B}_i^{(d)}$. Defining $\bar{n}_i = |g\rangle_i\langle g|$ and $n_i = |r\rangle_i\langle r|$, the nearest-neighbour projector is written as $\hat{A}_i = \prod_{\langle j,i\rangle} \bar{n}_j$, where $\langle\,.\,\rangle$ denotes nearest neighbours. The projector $\hat{B}_i^{(d)}$ sums over all configurations of the diagonal neighbours (indexed k_1, k_2, k_3, k_4) with d excitations:

$$\hat{B}_i^{(4)} = n_{k_1} n_{k_2} n_{k_3} n_{k_4} \quad (6)$$

$$\hat{B}_i^{(3)} = \bar{n}_{k_1} n_{k_2} n_{k_3} n_{k_4} + n_{k_1} \bar{n}_{k_2} n_{k_3} n_{k_4} + \ldots \quad (7)$$

$$\hat{B}_i^{(2)} = \bar{n}_{k_1} \bar{n}_{k_2} n_{k_3} n_{k_4} + \bar{n}_{k_1} n_{k_2} \bar{n}_{k_3} n_{k_4} + \ldots \quad (8)$$

These operators are used to construct the conditional Rydberg density

$$P^{(d)} = \frac{\sum_i \langle n_i \hat{\mathcal{O}}_i^{(d)} \rangle}{\sum_i \langle \hat{\mathcal{O}}_i^{(d)} \rangle}$$

which measures the probability of Rydberg excitation on site i surrounded by neighbouring-atom configurations for which $\hat{\mathcal{O}}_i^{(d)} = 1$.

To quantify coherences, we measure these conditional probabilities on their corresponding resonances, after a fixed quench with variable quench phase ϕ_q. For a single particle driven by the Hamiltonian $H = \Omega(\cos\phi_q \sigma_x + \sin\phi_q \sigma_y)/2 + \Delta\sigma_z/2$ for time τ, the resulting Heisenberg evolution is given by $\sigma_z' = U^\dagger \sigma_z U$, where $U = \mathrm{e}^{-\mathrm{i}H\tau}$. The resulting operator can be expressed as

$$\begin{aligned}\sigma_z' = {} & \tilde{\Omega}\sin 2\alpha(-\sigma_x\sin\phi_q + \sigma_y\cos\phi_q) \\ & + 2\tilde{\Delta}\tilde{\Omega}\sin^2\alpha(\sigma_x\cos\phi_q + \sigma_y\sin\phi_q) \\ & + (\cos^2\alpha - (1-2\tilde{\Delta}^2)\sin^2\alpha)\sigma_z\end{aligned} \quad (9)$$

where $\tilde{\Delta} = \Delta/\sqrt{\Delta^2+\Omega^2}$, $\tilde{\Omega} = \Omega/\sqrt{\Delta^2+\Omega^2}$ and $\alpha = \frac{1}{2}\tau\sqrt{\Delta^2+\Omega^2}$.

We fit the conditional probabilites $P^{(0)}$ and $P^{(4)}$ as a function of ϕ_q (Fig. 5d, e), taking Δ as the effective detuning from interaction-shifted resonance, and measuring $\langle\sigma_z'\rangle$ as a function of ϕ_q to extract the Bloch vector components $\langle\sigma_x\rangle$, $\langle\sigma_y\rangle$, $\langle\sigma_z\rangle$ on the two respective sublattices. For the (1,1) sublattice response, we model the evolution averaged over random detunings, due to ~15% fluctuations of the interaction shifts associated with thermal fluctuations in atomic positions, which broaden and weaken the spectroscopic response. For both sublattices we also include fluctuations in the calibrated pulse area (~10% due to low power used). The extracted fit values are $\sigma^{(0,0)}_{x,y,z} = -0.82(6), 0.25(2), -0.32(4)$ and $\sigma^{(1,1)}_{x,y,z} = -0.46(4), 0.01(1), 0.91(5)$.

Data availability

The data that support the findings of this study are available from the corresponding author on reasonable request.

60. Kim, D. et al. Large-scale uniform optical focus array generation with a phase spatial light modulator. *Opt. Lett.* **44**, 3178–3181 (2019).
61. Endres, M. et al. Atom-by-atom assembly of defect-free one-dimensional cold atom arrays. *Science* **354**, 1024–1027 (2016).
62. Lee, W., Kim, H. & Ahn, J. Defect-free atomic array formation using the Hungarian matching algorithm. *Phys. Rev. A* **95**, 053424 (2017).
63. Sheng, C. et al. Efficient preparation of 2D defect-free atom arrays with near-fewest sorting-atom moves. *Phys. Rev. Research* **3**, 023008 (2021).
64. Levine, H. et al. High-fidelity control and entanglement of Rydberg-atom qubits. *Phys. Rev. Lett.* **121**, 123603 (2018).
65. Bowman, D. et al. High-fidelity phase and amplitude control of phase-only computer generated holograms using conjugate gradient minimisation. *Opt. Express* **25**, 11692–11700 (2017).
66. Zupancic, P. et al. Ultra-precise holographic beam shaping for microscopic quantum control. *Opt. Express* **24**, 13881–13893 (2016).
67. Beterov, I. I., Ryabtsev, I. I., Tretyakov, D. B. & Entin, V. M. Quasiclassical calculations of blackbody-radiation-induced depopulation rates and effective lifetimes of Rydberg *nS*, *nP*, and *nD* alkali-metal atoms with $n \leq 80$. *Phys. Rev. A* **79**, 052504 (2009).
68. Bhattacharjee, S. M. & Seno, F. A measure of data collapse for scaling. *J. Phys. Math. Gen.* **34**, 6375 (2001).
69. Hasenbusch, M. Monte Carlo study of surface critical phenomena: the special point. *Phys. Rev. B* **84**, 134405 (2011).
70. White, S. R. Density matrix formulation for quantum renormalization groups. *Phys. Rev. Lett.* **69**, 2863 (1992).
71. White, S. R. Density-matrix algorithms for quantum renormalization groups. *Phys. Rev. B* **48**, 10345 (1993).
72. Stoudenmire, E. M. & White, S. R. Studying two-dimensional systems with the density matrix renormalization group. *Annu. Rev. Condens. Matter Phys.* **3**, 111–128 (2012).
73. Fishman, M., White, S. R. & Stoudenmire, E. M. The ITensor software library for tensor network calculations. Preprint at https://arxiv.org/abs/2007.14822 (2020).

Acknowledgements We thank many members of the Harvard AMO community, particularly E. Urbach, S. Dakoulas and J. Doyle for enabling safe and productive operation of our laboratories during 2020. We thank H. Bernien, D. Englund, M. Endres, N. Gemelke, D. Kim, P. Stark and A. Zibrov for discussions and experimental help. We acknowledge financial support from the Center for Ultracold Atoms, the US National Science Foundation, the Vannevar Bush Faculty Fellowship, the US Department of Energy (DE-SC0021013 and DOE Quantum Systems Accelerator Center, contract no. 7568717), the Office of Naval Research, the Army Research Office MURI and the DARPA ONISQ programme. T.T.W. acknowledges support from Gordon College. H.L. acknowledges support from the National Defense Science and Engineering Graduate (NDSEG) fellowship. G.S. acknowledges support from a fellowship from the Max Planck/Harvard Research Center for Quantum Optics. D.B. acknowledges support from the NSF Graduate Research Fellowship Program (grant DGE1745303) and the Fannie and John Hertz Foundation. W.W.H. is supported by the Moore Foundation's EPiQS Initiative grant no. GBMF4306, the NUS development grant AY2019/2020, and the Stanford Institute of Theoretical Physics. S.C. acknowledges support from the Miller Institute for Basic Research in Science. R.S. and S.S. were supported by the US Department of Energy under grant DE-SC0019030. The DMRG calculations were performed using the ITensor Library[73]. The computations in this paper were run on the FASRC Cannon cluster supported by the FAS Division of Science Research Computing Group at Harvard University.

Author contributions S.E., T.T.W., H.L., A.K., G.S, A.O. and D.B. contributed to building the experimental set-up, performed the measurements and analysed the data. Theoretical analysis was performed by R.S., H.P., W.W.H. and S.C. All work was supervised by S.S., M.G., V.V. and M.D.L. All authors discussed the results and contributed to the manuscript.

Competing interests M.G., V.V. and M.D.L. are co-founders and shareholders of QuEra Computing. A.K. and A.O. are shareholders of QuEra Computing. All other authors declare no competing interests.

Additional information

Supplementary information The online version contains supplementary material available at https://doi.org/10.1038/s41586-021-03582-4.

Correspondence and requests for materials should be addressed to M.D.L.

Peer review information *Nature* thanks the anonymous reviewer(s) for their contribution to the peer review of this work.

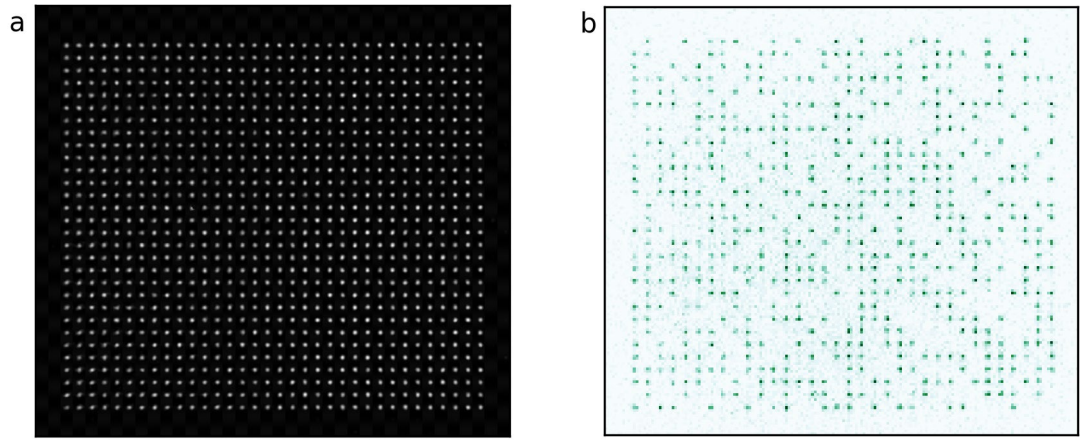

Extended Data Fig. 1 | Large arrays of optical tweezers. The experimental platform produces optical tweezer arrays with up to ~1,000 tweezers and ~50% loading probability per tweezer after 100 ms of magneto-optical trap loading time. **a**, Camera image of an array of 34 × 30 tweezers (1,020 traps), including aberration correction. **b**, Sample image of random loading into this tweezer array, with 543 loaded atoms. Atoms are detected on an EMCCD camera with fluorescence imaging.

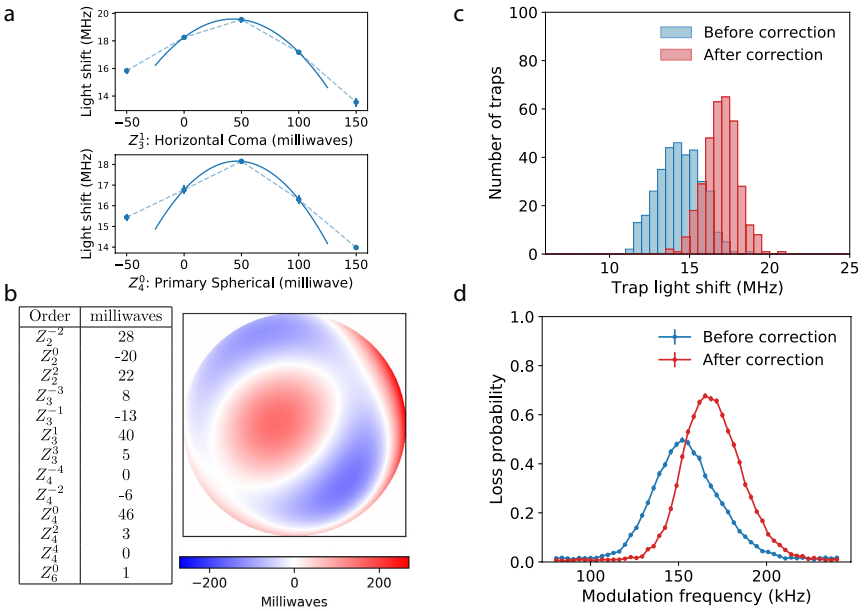

Order	milliwaves
Z_2^{-2}	28
Z_2^0	-20
Z_2^2	22
Z_3^{-3}	8
Z_3^{-1}	-13
Z_3^1	40
Z_3^3	5
Z_4^{-4}	0
Z_4^{-2}	-6
Z_4^0	46
Z_4^2	3
Z_4^4	0
Z_6^0	1

Extended Data Fig. 2 | Correcting for aberrations in the SLM tweezer array. The aberration correction procedure uses the orthogonality of Zernike polynomials and the fact that correcting aberrations increases tweezer light shifts on the atoms. To independently measure and correct each aberration type, Zernike polynomials are added with variable amplitude to the SLM phase hologram, with values optimized to maximize tweezer light shifts. **a**, Two common aberration types: horizontal coma (upper) and primary spherical (lower), for which ~50 milliwaves compensation on each reduces aberrations and results in higher-depth traps. **b**, Correcting for aberrations associated with the 13 lowest-order Zernike polynomials. The sum of all polynomials with their associated coefficients gives the total wavefront correction (RMS ~70 milliwaves) for our optical system, which is summed with the optical tweezer hologram on the SLM. **c**, Trap depths across a 26 × 13 trap array before and after correction for aberrations. Aberration correction results in tighter focusing (higher trap light shift) and improved homogeneity. Trap depths are measured by probing the light shift of each trap on the $|5S_{1/2}, F = 2\rangle \rightarrow |5P_{3/2}, F' = 2\rangle$ transition. **d**, Aberration correction also results in higher and more homogeneous trap frequencies across the array. Trap frequencies are measured by modulating tweezer depths at variable frequencies, resulting in parametric heating and atom loss when the modulation frequency is twice the radial trap frequency. The measurement after correction for aberrations shows a narrower spectrum and higher trap frequencies (averaged over the whole array).

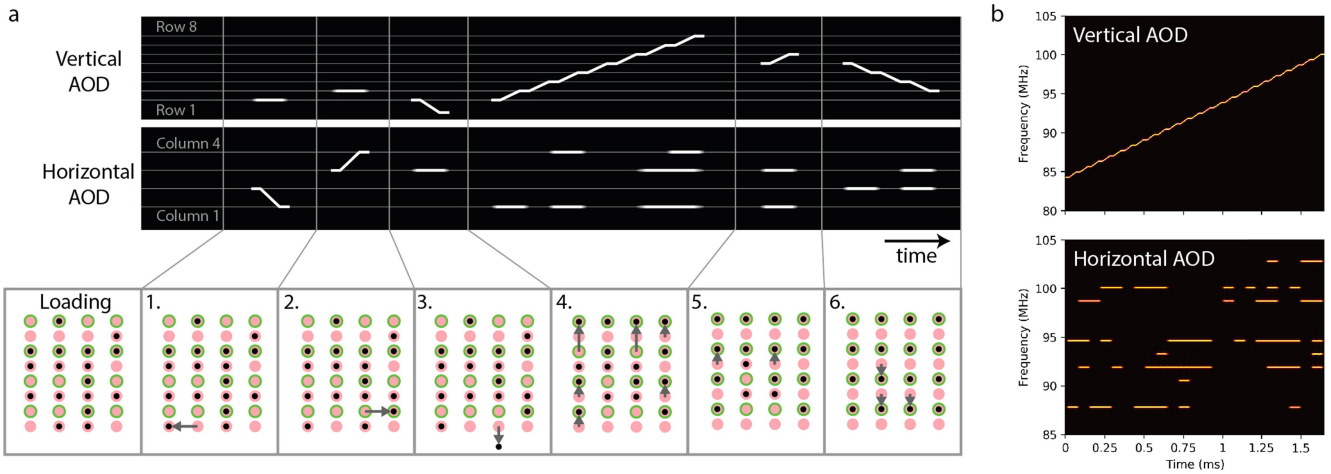

Extended Data Fig. 3 | Rearrangement protocol. a, Sample sequence of individual rearrangement steps. There are two pre-sorting moves (1, 2). Move 3 is the single ejection move. Moves 4–6 consist of parallel vertical sorting within each column, including both upward and downward moves. The upper panel illustrates the frequency spectrum of the waveform in the vertical and horizontal AODs during these moves, with the underlying grid corresponding to the calibrated frequencies that map to SLM array rows and columns. **b**, Spectrograms representing the horizontal and vertical AOD waveforms over the duration of a single vertical frequency scan during a realistic rearrangement procedure for a 26 × 13 array. The heat-maps show frequency spectra of the AOD waveforms over small time intervals during the scan.

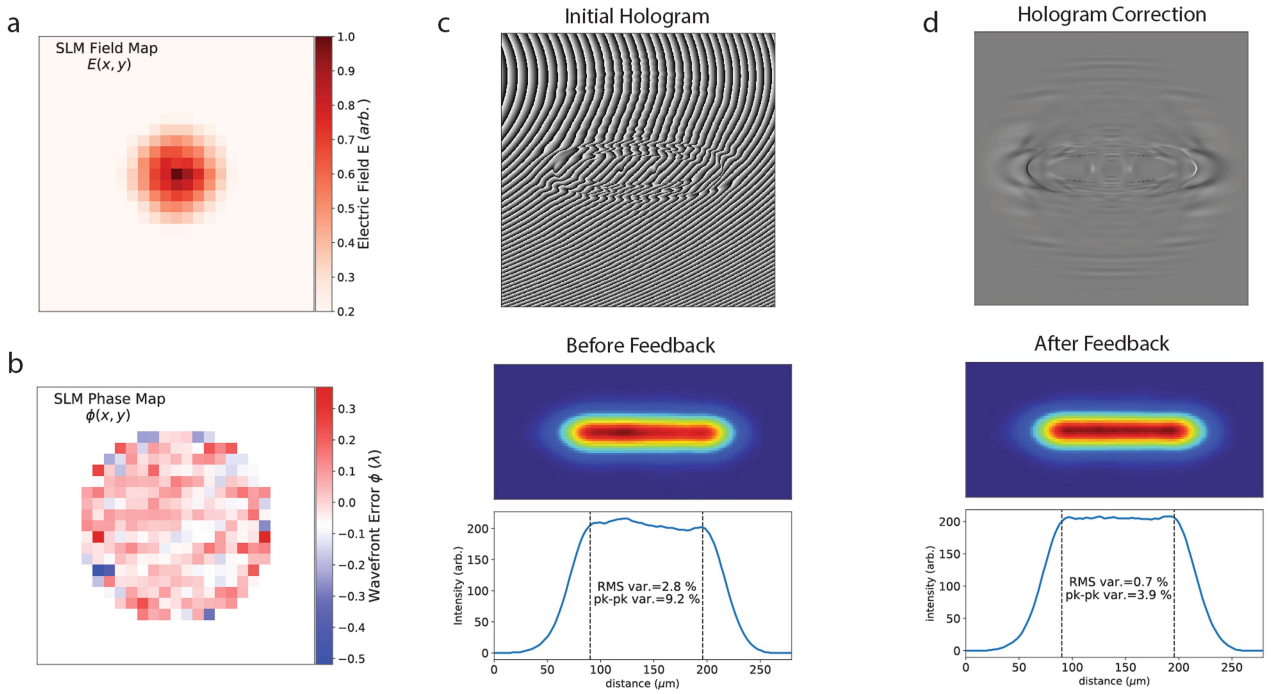

Extended Data Fig. 4 | Generating homogeneous Rydberg beams. **a**, Measured Gaussian-beam illumination on the SLM for shaping the 420-nm Rydberg beam. A Gaussian fit to these data is used as an input for the hologram optimization algorithm. **b**, Measured wavefront error through our optical system (after correction), showing a reduction of aberrations to $\lambda/100$. **c**, Computer-generated hologram for creating the 420-nm top-hat beam. **d**, Measured light intensity of the 420-nm top-hat beam (top), and the cross-section along where atoms will be positioned (bottom). Vertical lines denote the 105-μm region where the beam should be flat. **e**, Using the measured top-hat intensity, a phase correction is calculated for adding to the initial hologram. **f**, Resulting top-hat beam after feedback shows considerably improved homogeneity. pk–pk, peak to peak.

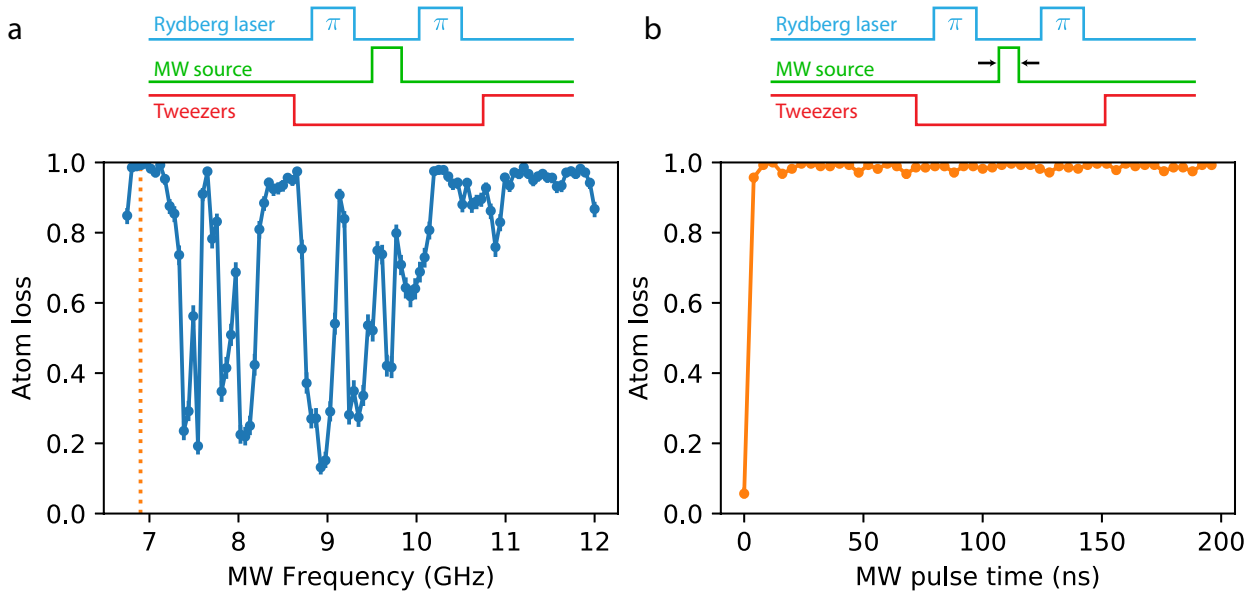

Extended Data Fig. 5 | Characterizing microwave-enhanced Rydberg detection fidelity. The effect of strong microwave (MW) pulses on Rydberg atoms is measured by preparing atoms in $|g\rangle$, exciting to $|r\rangle$ with a Rydberg π-pulse, and then applying the microwave pulse before de-exciting residual Rydberg atoms with a final Rydberg π-pulse. (The entire sequence occurs while tweezers are briefly turned off.) **a**, Broad resonances are observed with varying microwave frequency, corresponding to transitions from $|r\rangle = |70S\rangle$ to other Rydberg states. Note that the transitions to $|69P\rangle$ and $|70P\rangle$ are in the range of 10–12 GHz, and over this entire range there is strong transfer out of $|r\rangle$. Other resonances might be due to multiphoton effects. **b**, With fixed 6.9-GHz microwave frequency and varying pulse time, there is a rapid transfer out of the Rydberg state on the timescale of several nanoseconds. Over short timescales, there may be coherent oscillations that return population back to $|r\rangle$, so a 100-ns pulse is used for enhancement of loss signal of $|r\rangle$ in the experiment.

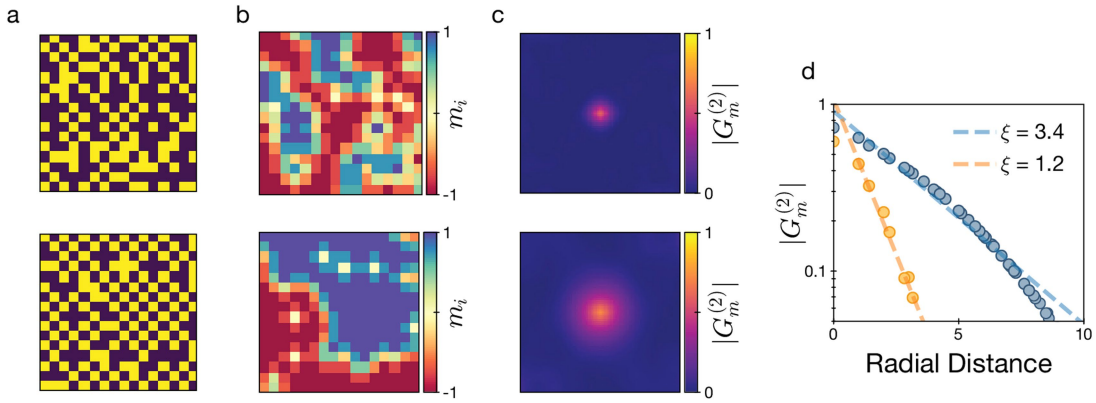

Extended Data Fig. 6 | Coarse-grained local staggered magnetization. **a**, Examples of Rydberg populations n_i after a faster (top) and slower (bottom) linear sweep. **b**, Corresponding coarse-grained local staggered magnetizations m_i clearly show larger extents of antiferromagnetically ordered domains (dark blue or dark red) for the slower sweep (bottom) than for the faster sweep (top), as expected from the Kibble–Zurek mechanism. **c**, Isotropic correlation functions $G_m^{(2)}$ for the corresponding coarse-grained local staggered magnetizations after a faster (top) or a slower (bottom) sweep. **d**, As a function of radial distance, correlations $G_m^{(2)}$ decay exponentially with a length scale corresponding to the correlation length ξ. The two decay curves correspond to faster (orange) and slower (blue) sweeps.

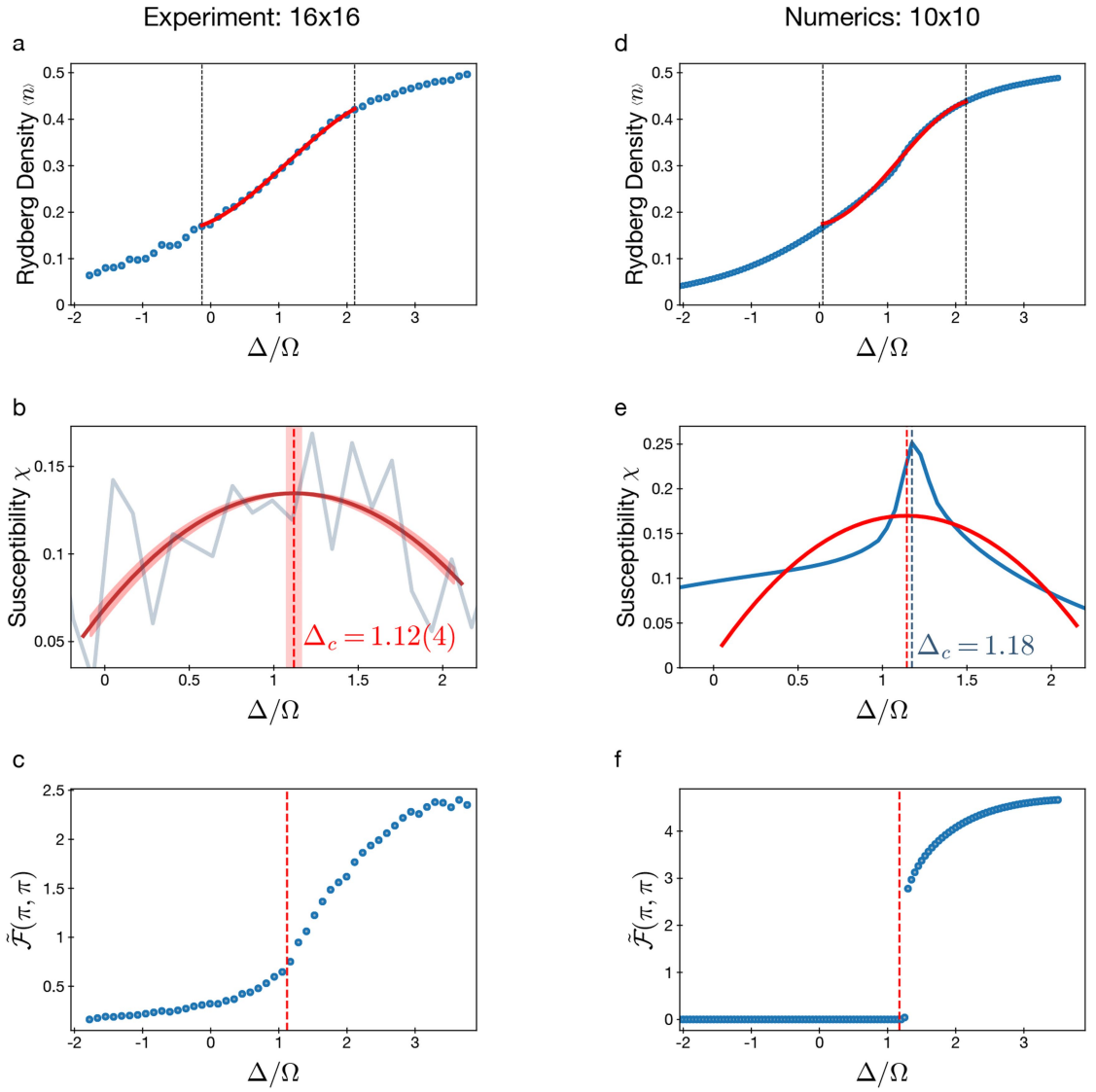

Extended Data Fig. 7 | Extracting the quantum critical point. a, The mean Rydberg excitation density $\langle n \rangle$ versus detuning Δ/Ω on a 16 × 16 array. The data are fitted within a window (dashed lines) to a cubic polynomial (red curve) as a means of smoothing the data. **b**, The peak in the numerical derivative of the fitted data (red curve) corresponds to the critical point $\Delta_c/\Omega = 1.12(4)$ (red shaded regions show uncertainty ranges, obtained from varying fit windows). In contrast, the point-by-point slope of the data (grey) is too noisy to be useful. **c**, Order parameter $\tilde{\mathcal{F}}(\pi, \pi)$ for the chequerboard phase versus Δ/Ω measured on a 16 × 16 array with the value of the critical point from **b** superimposed (red line), showing the clear growth of the order parameter after the critical point. **d**, DMRG simulations of $\langle n \rangle$ versus Δ/Ω on a 10 × 10 array. For comparison against the experimental fitting procedure, the data from numerics are also fitted to a cubic polynomial within the indicated window (dashed lines). **e**, The point-by-point slope of the numerical data (blue curve) has a peak at $\Delta_c/\Omega = 1.18$ (blue dashed line), in good agreement with the results (red dashed line) from both the numerical derivative of the cubic fit on the same data (red curve) and the result of the experiment. **f**, DMRG simulation of $\tilde{\mathcal{F}}(\pi, \pi)$ versus Δ/Ω, with the exact quantum critical point from numerics shown (red line).

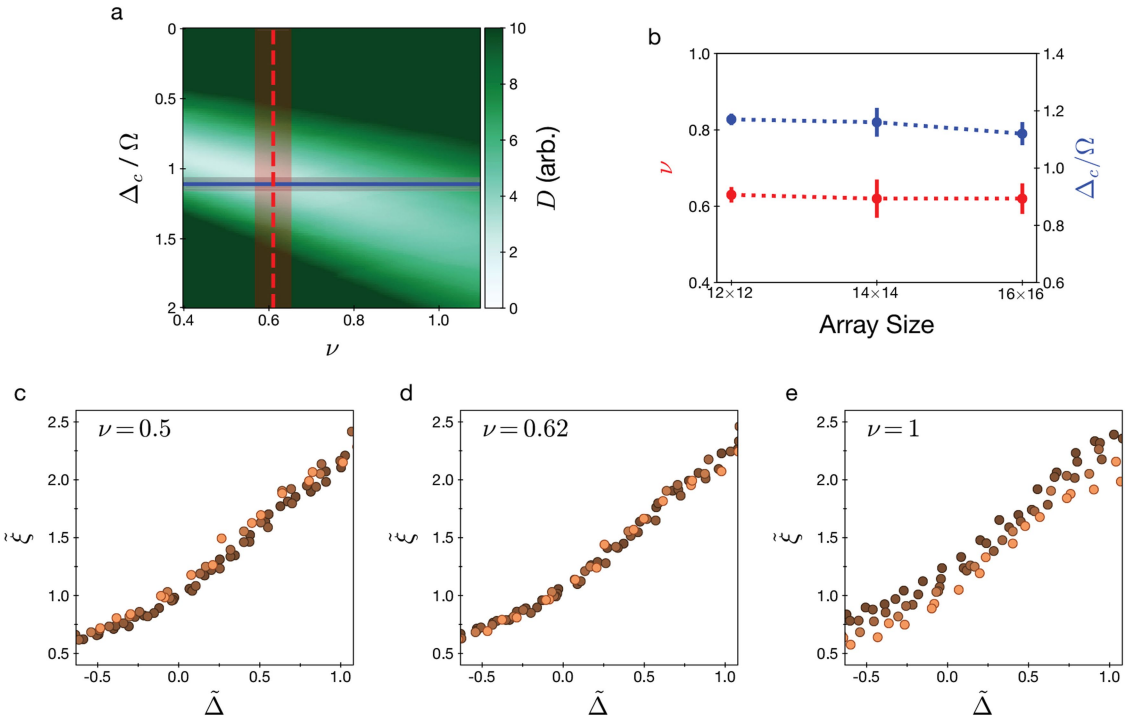

Extended Data Fig. 8 | Optimization of data collapse. a, Distance D between rescaled correlation length $\tilde{\xi}$ versus $\tilde{\Delta}$ curves depends on both the location of the quantum critical point Δ_c/Ω and on the correlation length critical exponent ν. The independently determined Δ_c/Ω (blue line, with uncertainty range in grey) and the experimentally extracted value of ν (dashed red line, with uncertainty range corresponding to the red shaded region) are marked on the plot. **b**, Our determination of ν (red) from data collapse around the independently determined Δ_c/Ω (blue) is consistent across arrays of different sizes. **c**–**e**, Data collapse is clearly better at the experimentally determined value ($\nu = 0.62$) as compared with the mean-field ($\nu = 0.5$) or the (1 + 1)D ($\nu = 1$) values. The horizontal extent of the data corresponds to the region of overlap of all rescaled datasets.